Title
Probing the Inelastic Interactions in Molecular Junctions by Scanning Tunneling Microscope

Permalink
https://escholarship.org/uc/item/5nw1d93s

Author
Xu, Chen

Publication Date
2016

Peer reviewed|Thesis/dissertation

UNIVERSITY OF CALIFORNIA,
IRVINE

Probing the Inelastic Interactions in Molecular Junctions by
Scanning Tunneling Microscope

DISSERTATION

submitted in partial satisfaction of the requirements
for the degree of

DOCTOR OF PHILOSOPHY

in Physics

by

Chen Xu

Dissertation Committee:
Professor Wilson Ho, Chair
Professor Ruqian Wu
Professor Ilya N. Krivorotov

2016

DEDICATION

To

Tingjia Chen

TABLE OF CONTENTS

LIST OF FIGURES

ACKNOWLEDGMENTS

CURRICULUM VITAE

Chen Xu

EDUCATION

2008	B.S. in Applied Physics
	University of Science and Technology of China
2009	M.S. in Physics
	University of California, Irvine
2009-13	Teaching Assistant
	University of California, Irvine
2009-16	Research Assistant
	University of California, Irvine
2016	Ph.D. in Physics
	University of California, Irvine

FIELD OF STUDY

Sub-Kelvin Scanning Tunneling Microscopy and Spectroscopy, Single Molecule Inelastic Electron Tunneling Spectroscopy, Single Molecule Inelastic Tunneling Probe

PUBICATION

Chen Xu, Chi-Lun Chiang, Zhumin Han and Wilson Ho, submitted, "On the Nature of Asymmetry in the Vibrational Line Shape of Single-Molecule Inelastic Electron Tunneling Spectroscopy with the STM"

Chi-Lun Chiang*, Chen Xu*, Zhumin Han* and Wilson Ho, "Real-Space Imaging of Molecular Structure and Chemical Bonding by Single-Molecule Inelastic Tunneling Probe", *Science* **334**, 885 (2014)
(* equal contribution)

ABSTRACT OF THE DISSERTATION

Probing the Inelastic Interactions in Molecular Junctions by
Scanning Tunneling Microscope

By

Chen Xu

Doctor of Philosophy in Physics

University of California, Irvine, 2016

Professor Wilson Ho, Chair

With a sub-Kelvin scanning tunneling microscope, the energy resolution of spectroscopy is improved dramatically. Detailed studies of finer features of spectrum become possible. The asymmetry in the line shape of carbon monoxide vibrational spectra is observed to correlate with the couplings of the molecule to the tip and substrates. The spin-vibronic coupling in the molecular junctions is revisited with two metal phthalocyanine molecules, unveiling sharp spin-vibronic peaks. Finally, thanks to the improved spectrum resolution, the bonding structure of the acyclic compounds molecules is surveyed with STM inelastic tunneling probe, expanding the capability of the innovative high resolution imaging technique.

Chapter 1 : Introduction

Since its invention, scanning tunneling microscope (STM) has been pioneering the surface science at the atomic scale. Spectroscopy has been its unique companion as a way to probe underlying mechanisms to surface phenomena. Improved resolution of spectra can always lead to new discoveries. The sub-Kelvin STM (mk-STM) was designed to improve the spectra resolution in order to further study electron-vibration interactions and electron-vibration-spin interactions in the molecular junctions. [1] Some literatures use the term electron-phonon interactions, [2] but here I refer to electron-vibration interactions, or vibronic coupling to minimize ambiguity.

High resolution spectroscopy here is defined with respect to spectra obtained with an STM system of 4.2 K or above. By using a Helium-3 cooling stage, the junction temperature can be effectively lowered below 1 K. These experiments are made possible by the well-established stably-operated sub-Kelvin STM system. The 600mK junction temperature further extenuates the thermal fluctuation which allows a finer bias modulation and eventually resolves more detailed spectrum structures.

On the way to the realization of molecular electronics, the vibration degree of freedom is inevitable yet interesting to investigate. Among numerous experimental set-ups, STM is the only one that is able to ascertain the existence of

single molecule inside a junction. [3] Ho group has been specialized in the area of electron-vibration interaction with STM molecular junctions since 1998. Being different from EELS or any other techniques, the way that STM characterizes single molecule vibration is through probing its interplay with the tunneling electrons.

The electron-vibration interaction will come into play when the time it takes a tunneling electron to interact with local vibrational modes is comparable to the transversal time which it takes the electron to travel from tip to the substrate, i.e.

$$\frac{\hbar}{\lambda} \sim \frac{\hbar}{\sqrt{\Delta E^2 + \Gamma^2}}$$

where $\hbar$ is the Plank constant, λ is the vibronic coupling constant, ΔE is the energy difference between the leads' Fermi energy and the relevant molecular orbital (HOMO or LUMO), and Γ is the metal-molecule electronic coupling independent of energy. The STM-IETS studied here is in the weak electron-vibration coupling limit. The 'weak' coupling λ here is defined as it is small relative to ΔE and Γ. In contrary, the spin-vibronic coupling is in the regime where ΔE and Γ is small in comparison with λ. This is also referred as resonant inelastic electron tunneling regime sometimes. [4]

To date, the discussion of STM-IETS application has mainly focused on the spatial resolution and the spectral energy and intensity. [5,6] With the sub-Kelvin STM, the resolution of d^2I/dV^2 spectrum is significantly improved. This

improvement leads to the revelation of the line shape of STM-IETS. Chapter 2 focuses on the study of STM-IETS line shape, which we discovered a controllable way to tune the IETS lineshape by molecular manipulation. The dependence of the line shape on the molecule's asymmetric couplings in the tunnel junction is corroborated by theoretical simulation which further validates the mechanisms of inelastic electron tunneling.

Vibronic coupling in single molecule has been under intensive research for years. [7–14] However, additional influence resulting from the spin degree of freedom has been lack of investigation owing to complexities in experimental design including the needs of ultra-low temperature and high magnetic field. [1,15] The improved resolution of the dI/dV makes the investigation on spin-vibronic coupling possible. Chapter 3 focuses on the interaction between spin and vibration in molecular junctions by surveying Copper Phthalocyanine (CuPc) and Cobalt Phthalocyanine (CoPc) adsorbed on aluminum oxide. We discovered that although the spin-flip IETS only confirms a net 1/2 single spin on CoPc and zero net spin on CuPc, the spin-vibronic signature is found for both CoPc and CuPc.

High resolution STM-IETS also makes the monitoring of the shift of IETS peak possible, resulting in the invention of the inelastic tunneling probe technique which is able to image the bonding structure of molecules. By recording the d^2I/dV^2 signal of a carbon monoxide molecule attached to the tip apex, the bonding structure of molecule can be resolved, which is impossible

without the high resolution IETS. [16] To date, applications of molecular structure imaging, including NC-AFM and itProbe, have been mainly confined to the study of cyclic molecules. [16–23] In Chapter 4 we demonstrate the extension of itProbe to investigate acyclic ethylene molecules adsorbed on Ag(110) surface and particularly reveal the three dimensional variations of the potential energy surface.

Chapter 5 is devoted to conclusion and prospects, which illustrates that the spin-flip IETS is also able to function as a kind of itProbe that when scanning across a subject molecule, the local variated magnetic field will affects the energy to flip a spin and thus produce a map related to magnetic field.

Bibliography

[1]   U. Ham and W. Ho, Physical Review Letters **108**, 106803 (2012).

[2]   M. Galperin, M. A. Ratner, and A. Nitzan, The Journal of Chemical Physics **121**, 11965 (2004).

[3]   W. Ho, The Journal of Chemical Physics **117**, 11033 (2002).

[4]   J. Cuevas and E. Scheer, *Molecular Electronics: An Introduction to Theory and Experiment* (World Scientific, 2010).

[5]   A. Baratoff and B. N. J. Persson, Journal of Vacuum Science & Technology A: Vacuum, Surfaces, and Films **6**, 331 (1988).

[6]   B. C. Stipe, M. A. Rezaei, and W. Ho, Science **280**, 1732 (1998).

[7]   H. Park, J. Park, A. Lim, E. Anderson, A. Alivisatos, and P. McEuen, Nature **407**, 57 (2000).

[8]   S. Wu, G. Nazin, X. Chen, X. Qiu, and W. Ho, Physical Review Letters **93**, 236802 (2004).

[9]   G. Nazin, S. Wu, and W. Ho, Proceedings of the National Academy of Sciences **102**, 8832 (2005).

[10]   N. Ogawa, G. Mikaelian, and W. Ho, Physical Review Letters **98**, 166103 (2007).

[11]   G. Nazin, X. Qiu, and W. Ho, The Journal of Chemical Physics **122**, 181105 (2005).

[12]   G. Nazin, X. Qiu, and W. Ho, Physical Review Letters **95**, 166103 (2005).

[13]   X. Qiu, G. Nazin, and W. Ho, Physical Review Letters **92**, 206102 (2004).

[14]   H. Lee, J. Lee, and W. Ho, ChemPhysChem **6**, 971 (2005).

[15]   Y. Fu, T. Zhang, S. Ji, X. Chen, X. Ma, J. Jia, and Q. Xue, Physical Review Letters **103**, 257202 (2009).

[16]   C. Chiang, C. Xu, Z. Han, and W. Ho, Science **344**, 885 (2014).

[17]   R. Temirov, S. Soubatch, O. Neucheva, A. Lassise, and F. Tautz, New Journal of Physics **10**, 053012 (2008).

[18]   L. Gross, F. Mohn, N. Moll, P. Liljeroth, and G. Meyer, Science **325**, 1110 (2009).

[19]   C. Weiss, C. Wagner, R. Temirov, and S. F. Tautz, Journal of the American Chemical Society **132**, 11864 (2010).

[20]   L. Gross, F. Mohn, N. Moll, B. Schuler, A. Criado, E. Guitián, D. Peña, A. Gourdon, and G. Meyer, Science **337**, 1326 (2012).

[21]   D. Oteyza, P. Gorman, Y.-C. Chen, S. Wickenburg, A. Riss, D. J. Mowbray, G. Etkin, Z. Pedramrazi, H.-Z. Tsai, A. Rubio, M. Crommie, and F. Fischer, Science **340**, 1434 (2013).

[22]   J. Zhang, P. Chen, B. Yuan, W. Ji, Z. Cheng, and X. Qiu, Science **342**, 611 (2013).

[23]   B. Schuler, S. Fatayer, F. Mohn, N. Moll, N. Pavliček, G. Meyer, D. Peña, and L. Gross, Nature Chemistry **8**, 220 (2016).

Chapter 2 : On the Nature of Asymmetry in the Vibrational Line Shape of Single-Molecule Inelastic Electron Tunneling Spectroscopy with the STM

2.1 Abstract

Single molecule vibrational spectroscopy and microscopy has been demonstrated in 1998 by inelastic electron tunneling with the scanning tunneling microscope (STM). To date, the discussion of its application has mainly focused on the spatial resolution and the spectral energy and intensity. Here we report on the vibrational line shape for a single carbon monoxide molecule that qualitatively exhibits inversion symmetry when it is transferred from the surface to the tip. The dependence of the line shape on the molecule's asymmetric couplings in the tunnel junction can be understood from theoretical simulation and further validates the mechanisms of inelastic electron tunneling.

2.2 Article

Inelastic electron tunneling spectroscopy (IETS) provides an excitation spectrum of vibrational modes by recording the small changes in the differential conductance as the voltage is ramped across the vibrational energy thresholds [1-4]. The combination of lock-in technology and stability of the tunneling gap in the scanning tunneling microscope (STM) enables IETS measurement of single molecules [4]. The vibrational energy is obtained from the peak position while the intensity is proportional to the vibrational excitation cross section [4, 5]. The line shape is more subtle and has not been resolved due to spectral broadening by the tip-sample temperature of the tunnel junction and amplitude of the lock-in modulation voltage [6-8]. However, the line shape contains information on the electron-vibration, the molecule-tip, and the molecule-substrate coupling strengths in the inelastic tunneling process [5, 9-11].

Vibrational IETS signatures of molecular junctions can appear as peaks [4, 12], dips [13, 14], and skewed features [15,16]. The origin of these various line shapes has been attributed to the interference between elastic and inelastic tunneling [11, 17-19]. However, the measured change in the differential conductance in IETS arises from the convolution of the elastic (negative change) and inelastic (positive change) channels that cannot be separated in the experiment. The onset of the inelastic channel influences the elastic channel and the measured change is the sum of the changes in both channels. Among all the theoretical efforts that have addressed the diverse line shapes observed in the

vibrational IETS, the single channel model stands out for its simplicity and generality [5,9,10,17,20,21]. Within this model, the line shape in IETS can result from the correlation between the molecular resonance level in the tunnel junction and the molecule-tip (Γ_t) and molecule-substrate (Γ_s) couplings. But gating a single molecule within the STM junction to shift the resonance level is a difficult task, and tuning Γ_t by changing the gap between the tip and adsorbed molecule does not produce significant changes in the IETS line shape because typically $\Gamma_t \ll \Gamma_s$ [22].

There is an extraordinary difference between Γ_s and Γ_t in the STM junction for molecules adsorbed on metal surfaces. Therefore, instead of tuning the tip-molecule tunneling gap or devising a gate electrode, the two opposing extremes ($\Gamma_s \gg \Gamma_t$ and $\Gamma_s \ll \Gamma_t$) can be realized in the STM by transferring the CO from the surface to the tip in a controlled manipulation. Furthermore, high energy resolution is required for resolving the line shape with a sub-Kelvin STM. The effects of the asymmetric tunnel junction on STM-IETS can therefore be determined, providing a deeper understanding of the line shape and the nature of inelastic tunneling.

The measurement by IETS was carried out with a home-built ultrahigh vacuum STM operated at ~ 600 mK and a base pressure of $\sim 5 \times 10^{-11}$ torr [23-25]. The Au(110) and Cu(100) surfaces and Ag tips were prepared by repeated cycles of sputtering and annealing. Dosing of CO molecules to achieve ~ 0.05 monolayer coverage on the Au(110) or Cu(100) surface was carried out at ~ 28 K.

Under typical imaging conditions of 1 nA tunneling current and 10 mV sample bias, the topography of CO reveals adsorption on the atop site as a round protrusion on the Au(110) surface but a round depression on the Cu(100) surface. Spectra were normally recorded with the tip positioned over the center of these round depressions or protrusions. Tips were conditioned by occasional field emissions at ~ 5 V and repeated poking into the metal surface to produce sharp and stable tip configurations. Following these treatments, the apex of the Ag tip is coated by substrate atoms. This was verified by observing the vibrational spectrum for a CO terminated tip measured over the bare Au(110) surface to be that of a CO adsorbed on the surface and measured by a metal tip [26]. Similarly, the Ag tip became coated with Cu atoms after poking into the Cu(100) surface, although we were not able to transfer CO from the Cu(100) surface to the tip.

There are four hindered vibrational modes for CO adsorbed on the atop site, besides the internal stretch and bouncing mode against the surface, as shown in Figure 2.1 a-d. For a surface with low symmetry, such as the Au(110) surface in Figure 2.1 e, the hindered translational mode (HT-mode) and the hindered rotational mode (HR-mode) have different energies. These two modes become degenerate when CO molecules are adsorbed on a high symmetry surface, such as the Cu(100) surface in Figure 2.1 f [12,27].

Figure 2.1: Adsorption of CO on surfaces with different symmetry. (a-d) Schematic diagrams showing the six vibrational modes of CO adsorbed on metal surfaces (the corresponding motions perpendicular to the plane of the paper for the hindered rotational (HR) mode in (c) and hindered translational (HT) mode in (d) are not shown.) Top view of (e) Cu(100) and (f) Au(110) surfaces with an isolated CO molecule adsorbed on top of a surface atom. The surface anisotropy of Au(110) lifts the degeneracy of the HT-mode and the HR-mode which are doubly degenerate on the Cu(100) surface.

(a) (b) (c) (d)

(e) $[1\bar{1}0]$ $[001]$

(f) $[0\bar{1}1]$ $[011]$

Au(110)   Cu(100)
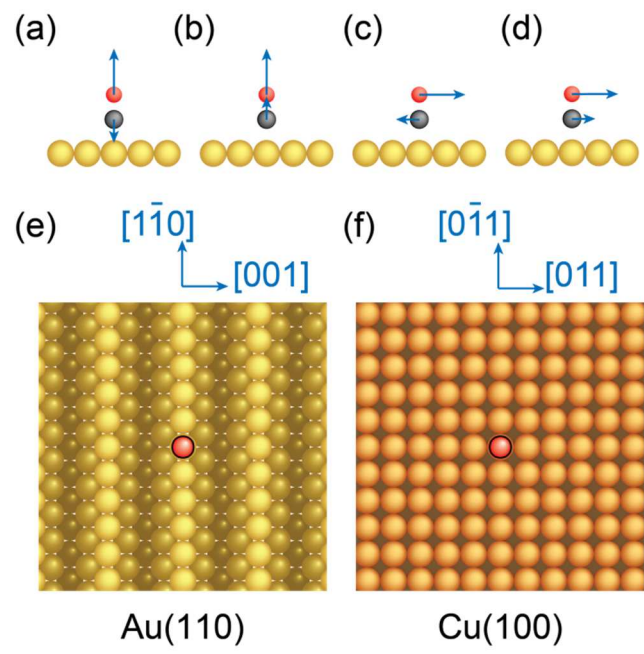
A STM-IETS spectrum for a single CO molecule adsorbed on Au(110) surface is shown in Figure 2.2 a and reveals both the HR-mode and the HT-mode. A splitting is found for the HR-modes due to the lifting of the degeneracy, with one peak at 30.8 meV (HR1 mode) and the other at 32.7 meV (HR2 mode). (The hindered translational (HT) mode is also split by ~0.8 meV and requires lower modulation bias voltage for its resolution.) The central features at ±1 meV are associated with the zero bias differential conductance (dI/dV) dip (ZBCD). This dip in dI/dV is attributed to the effect of the Coulomb blockade or equivalently the reduction in current for low energy charged particles due to the space charge effect [28]. Furthermore, a difference is observed for the intensity of the HR-doublet. Most strikingly, the HR2 mode is more intense at positive bias, but the HR1 mode is more intense at negative bias. In contrast, it is expected for a symmetric junction that the molecular vibration would be similarly excited for electrons tunneling from the tip (positive bias) or from the substrate (negative bias) so that the relative intensity of the two HR modes should be independent of the bias polarity. The dependence of the relative intensity on the bias polarity has its origin in the asymmetry of the tunneling junction.

Figure. 2.2: The asymmetric tunneling gap with CO adsorbed on two-fold symmetric Au(110) surface and to the tip. (a) Vibrational STM-IETS d^2I/dV^2 spectrum taken with Au coated tip for single CO adsorbed on the atop site of the row of atoms. The upper curve (blue) is recorded over a CO molecule; the lower curve (red) is over a row of the Au(110) surface (spectrum is similar over the trough between two rows). Bias modulation: 1 mV at 471 Hz, and tunneling gap set point: $V = 20$ mV and $I = 1$ nA. The doublet for the HR-mode at 30.8 meV and 32.7 meV shows reversed relative peak intensities for opposite bias polarities due to asymmetry in the line shape. The green curve in the inset is for the doublet of the HT-mode at 4.1 meV and 4.9 meV, taken with modulation 300 μV at 471 Hz and tunneling gap set point: $V = 10$ mV and $I = 1$ nA. The line shape of the HT-mode is obscured by the zero bias conductance dip (ZBCD) at 1 meV (as shown isolated in the spectrum taken over the Au surface.) (b) STM-IETS with CO-terminated tip measured over the Au(110) surface. Bias modulation: 1 mV at 471 Hz, and tunneling gap set point: $V = 10$ mV and $I = 1$ nA. The energy of the HR-mode at 31.3 meV is the same as the average of the doublet for a Au-coated tip over a CO on the Au surface, indicating that the tip is coated with Au atoms. The line shape for the HR-mode is asymmetric, but is obscured by the ZBCD for the HT-mode. Schematic diagrams of the geometric configurations for (c) the metal tip probing single CO on Au(110) surface and (d) the CO-terminated tip probing Au(110) surface. (e) STM topography of CO adsorbed on Au(110) surface (20 Å × 20 Å), taken with a metal tip. Set point: $V = 10$ mV and $I = 1$ nA. (f) STM topography of CO-terminated tip probing the Au(110) surface (20 Å × 20 Å). Set point: $V = 2$ mV and $I = 1$ nA. Surface atoms are resolved.

15
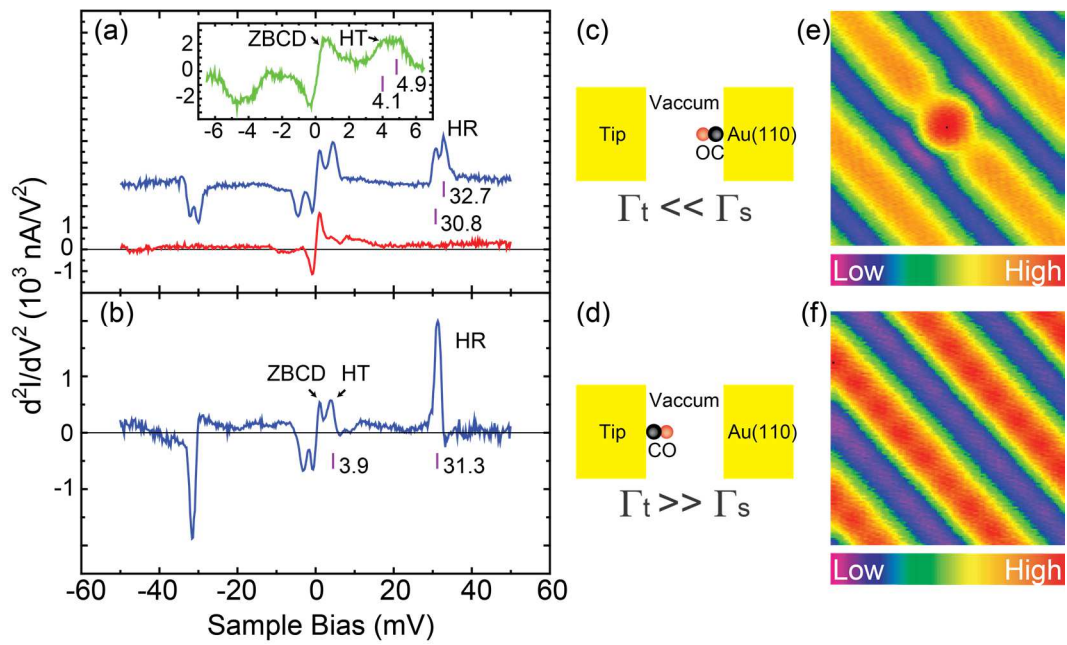
The vibrational spectrum by STM-IETS with the CO-terminated tip positioned over a surface Au atom is shown in Figure 2.2 b, revealing the CO vibrational excitations at 3.9 meV (HT-mode) and 31.3 meV (HR-mode). The modes are present at all positions of the surface and close in energies as those for CO adsorbed on top of an Au atom (atop site) of the Au(110) surface (Figure 2.2 a), confirming that the tip is coated with Au atoms and terminated with a CO molecule. The two HR-modes are not split, suggesting that the CO is adsorbed in a high symmetry site of the tip. Furthermore, the line shape of the HR-mode is not symmetric with falling tail at left side and a shallow dip at right side of the peak at positive bias, but with rising tail at the left side and a shallow peak at the right side of the dip at negative bias. This asymmetry could explain the different intensity of the HR-doublet for CO on the Au(110) surface (Figure 2.2 a) as resulting from the sum of two asymmetric line shapes of similar intensity in the doublet.

The schematic in Figure 2.2 c and Figure 2.2 d show that CO is coupled with different strengths to the substrate and the tip, depending on the side of the junction to which it is adsorbed. When CO is adsorbed on the surface, the rates yield $\Gamma_t \ll \Gamma_s$, as shown in Figure 2.2 c. The coupling of the CO to the tip is strengthened ($\Gamma_t \gg \Gamma_s$) when it is transferred from the surface to the tip, as shown schematically in Figure 2.2 d. The resolution in the topographic image is enhanced with a CO-terminated tip, as are displayed for a bare (Figure 2.2 e) and a CO-terminated tip (Figure 2.2 f). The observation of atomic resolution for the

substrate surface indicates a functionalized tip, in addition to the vibrational signatures of CO by IETS.

The understanding of asymmetry in the STM-IETS line shape can be further validated by analyzing CO molecules adsorbed on four-fold symmetric Cu(100) surface with a Cu-coated Ag tip, as shown in Figure 2.3 a and Figure 2.3 b. Both the HT-doublet and the HR-doublet of CO become degenerate and are detected at 4.1 meV and 35.1 meV, respectively, as shown by the IETS spectrum in Figure 2.3 c. The line shape for the HR-mode is notably asymmetric. Since the CO molecule couples more strongly to the substrate than to the tip ($\Gamma_s >> \Gamma_t$), the asymmetry in the line shape of the HR-mode is on the opposite side of the peak at positive bias compared to that with CO on the tip in Figure 2.2 b (and similarly for the dip at negative bias.)

Figure. 2.3: Adsorption of CO on four-fold symmetric Cu(100) probed with a metal tip. (a) Schematic diagram of the tunneling gap configuration. (b) STM topographic image of CO (20 Å × 20 Å). Tunneling gap set point: $V = 4$ mV and $I = 4$ nA. (c) STM-IETS over CO (lower spectrum in blue). ZBCD is observed over the substrate (upper spectrum in red). Bias modulation: 1 mV at 471 Hz, and tunneling gap set point: $V = 20$ mV and $I = 1$ nA.
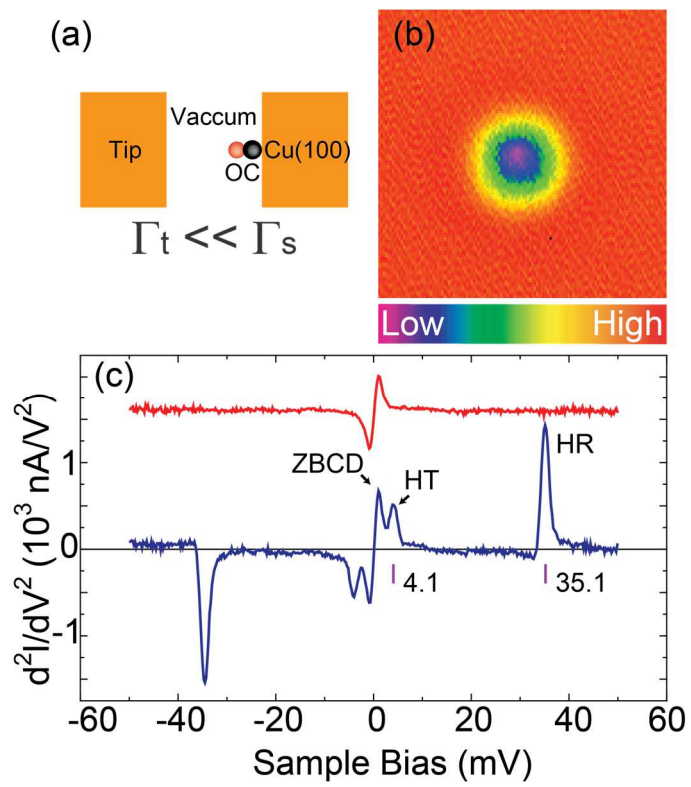
The asymmetry in the line shape can be explained by simulation using the single channel model [9,10,20]. Based on the non-equilibrium Green's function formalism and the approximation by the lowest order expansion, the tunneling current can be divided into a Landauer term and two universal function terms I^{sym} and I^{asym}, where dI^{sym}/dV is an even function of the bias and dI^{asym}/dV is an odd function of the bias. The Landauer term describes the trivial linear dependency of tunneling current on bias and its second derivative is zero. The dI^{asym}/dV term depends on the balance between Γ_s and Γ_t; it completely vanishes when $\Gamma_s = \Gamma_t$. The asymmetry in the line shape changes from one side to the other of the d^2I/dV^2 peak or dip, as shown in Figure 2.4 a and Figure 2.4 b for $\Gamma_s \gg \Gamma_t$ and $\Gamma_s \ll \Gamma_t$. The parameters are chosen such that the closest resonance lies away from the Fermi surface (off-resonance case) [22]. Detail of the simulation can be found in the supplemental material [29]. As illustrated in Figure 2.4 , the STM-IETS spectrum is the addition of d^2I^{sym}/dV^2 and d^2I^{asym}/dV^2, where d^2I^{sym}/dV^2 yields the outline of the spectrum while d^2I^{asym}/dV^2 produces the small asymmetric correction. With the couplings changes from $\Gamma_s \gg \Gamma_t$ to $\Gamma_t \gg \Gamma_s$, the outline of IETS stays the same while the small asymmetric correction changes in sign:

$$\frac{d^2I^{sym}(\Gamma_t, \Gamma_s)}{dV^2} = \frac{d^2I^{sym}(\Gamma_s, \Gamma_t)}{dV^2}$$

$$\frac{d^2I^{asym}(\Gamma_t, \Gamma_s)}{dV^2} = -\frac{d^2I^{asym}(\Gamma_s, \Gamma_t)}{dV^2}$$

Therefore, the asymmetry in the IETS line shape changes as Γ_s and Γ_t reverse in strength.

Figure. 2.4: Simulation of STM-IETS using the single channel model from Ref. 20. Refer to the online supplemental materials for more details. Simulation of CO on Cu(100): (a) $\Gamma_s \gg \Gamma_t$, and (b) $\Gamma_t \gg \Gamma_s$. The red dashed curve is d^2I^{sym}/dV^2 and the black dotted curve is d^2I^{asym}/dV^2. The d^2I^{sym}/dV^2 remains the same and d^2I^{asym}/dV^2 changes sign when Γ_s and Γ_t are reversed in relative strength. The sum of d^2I^{sym}/dV^2 and $d^2I^{asym}/dV2$ is shown as the solid curve in blue. (c) and (d) Simulation of the doublet for the HR mode in STM-IETS for metal tip probing CO adsorbed on Au(110) surface. The red and black curves represent individual spectrum by IETS for the two HR modes, taken to be equal intensity, with the sum of the two spectra shown by the blue curve. The asymmetry in the line shape for each HR mode leads to the overall asymmetry of the sum.
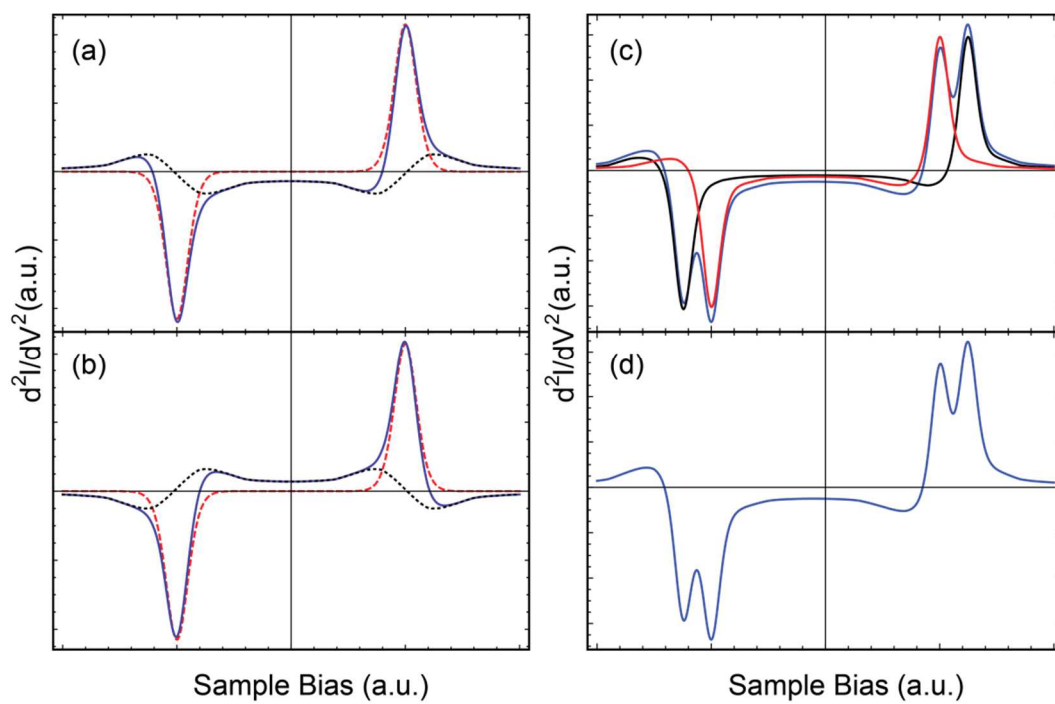
The simulation of the doublet in the IETS spectrum for CO adsorbed on Au(110), a surface of lower symmetry (Figure 2.4 c), provides an explanation to the observed relative intensity of the two peaks at positive and negative biases. It should be noted that in the simulation, the exact values of Γ_s and Γ_t are chose arbitrarily and only their relative strengths can be experimentally deduced.

According to the single channel model, the dI^{sym}/dV and dI^{asym}/dV are related to the imaginary and real parts of the self-energy of the adsorbate, which are correlated by the Kramers–Kronig relations [17]. Furthermore, the symmetric term contains both the inelastic and elastic contributions, while the connection is not clear for the antisymmetric term [10,20]. A similar line shape asymmetry can also be observed in the IETS spectrum for a bare tip probing a CO $\sqrt{3} \times \sqrt{3}$ array adsorbed on the Cu(111) surface and the asymmetry changes when the tip was positioned over a chevron-shaped CO assembly [30]. The reason for such a change may be attributed to the variation of the adsorbate resonance, but the exact mechanism still needs further investigation.

In summary, we report the existence of vibrational asymmetry in the off-resonance STM-IETS that can only be resolved with high energy resolution at below 1 K. Such measurements reveal that the line shape asymmetry results from the difference in strength between the molecule-tip coupling Γ_t and the molecule-substrate coupling Γ_s. Based on the non-equilibrium Green's function formalism and the approximation of the lowest order expansion, the single channel model was adopted to simulate the line shape of the IETS spectra, and a consistent

agreement between experiment and theory has been achieved. The confirmation of the spectral asymmetry in STM-IETS provides a deeper understanding into the mechanisms of vibrationally inelastic electron tunneling.

2.3 Bibliography

[1] R.C. Jaklevic and J. Lambe, Physical Review Letters **17**, 1139 (1966).

[2] G. Binnig, N. Garcia, and H. Rohrer, Physical Review B **32**, 1336 (1985).

[3] B. N. J. Persson and A. Baratoff, Physical Review Letters **59**, 339 (1987).

[4] B. C. Stipe, M. A. Rezaei, and W. Ho, Science **280**, 1732 (1998).

[5] A. Baratoff and B. N. J. Persson, Journal of Vacuum Science and Technology A **6**, 331 (1988).

[6] L. J. Lauhon and W. Ho, Review of Scientific Instruments **72**, 216 (2001).

[7] S. Paavilainen and M. Persson, Physical Review B **74**, 085417 (2006).

[8] S. Monturet, M. Alducin, and N. Lorente, Physical Review B **82**, 085447 (2010).

[9] M. Paulsson, T. Frederiksen, and M. Brandbyge, Physical Review B **72**, 201101 (2005).

[10] M. Paulsson, T. Frederiksen, and M. Brandbyge, Journal of Physics: Conference Series **35**, 247 (2006).

[11] M. Galperin, M. A. Ratner, and A. Nitzan, Journal of Chemical Physics. **121**, 11965 (2004).

[12] L. J. Lauhon and W. Ho, Physical Review B **60**, R8525 (1999).

[13] J. R. Hahn, H. J. Lee, and W. Ho, Physical Review Letters **85**, 1914 (2000).

[14] R. H. M. Smit, Y. Noat, C. Untiedt, N. D. Lang, M. C. van Hemert, and J. M. van Ruitenbeek, Nature **419**, 906 (2002).

[15] W. Y. Wang, T. Lee, I. Kretzschmar, and M. A. Reed, Nano Letters **4**, 643 (2004).

[16] S. Li, A. Yu, F. Toledo, Z. Han, H. Wang, H. He, R. Wu, and W. Ho, Physical Review Letters **111**, 146102 (2013).

[17] H. Ueba, T. Mii, and S. G. Tikhodeev, Surface Science **601**, 5220 (2007).

[18] N. Lorente and M. Persson, Physical Review Letters **85**, 2997 (2000).

[19] M. Persson, Philosophical Transactions of the Royal Society A: Mathematical, Physical and Engineering Sciences **362**, 1173 (2004).

[20] M. Paulsson, T. Frederiksen, H. Ueba, N. Lorente, and M. Brandbyge, Physical Review Letters **100**, 226604 (2008).

[21] M. Galperin, M. Ratner, and A. Nitzan, Nano Letters **4**, 1605 (2004).

[22] L. Vitali, R. Ohmann, K. Kern, A. Garcia-Lekue, T. Frederiksen, D. Sanchez-Portal, and A. Arnau, Nano Letters **10**, 657 (2010).

[23] U. Ham and W. Ho, Physical Review Letters **108**, 106803 (2012).

[24] U. Ham and W. Ho, Journal of Chemical Physics. **138**, 074703 (2013).

[25] C.L. Chiang, C. Xu, Z. Han, and W. Ho, Science **344**, 885 (2014).

[26] Here the spectrum is not exactly the same as that for CO on Au(110), but it is definitely not the spectrum for CO on Ag surface, where the hindered rotational mode is around 20 meV.

[27] J. Ahner, D. Mocuta, R. D. Ramsier, and J. T. Yates, Jr., Physical Review Letters **79**, 1889 (1997).

[28] R. Egerton, Reports on Progress in Physics **72**, 016502 (2008).

[29] See the supplementary material for details, the code is also available at

https://github.com/iets-lineshape/simulation

[30] A. J. Heinrich, C. Lutz, J. Gupta, and D. Eigler, Science **298**, 1381 (2002).

Chapter 3 : Probing the Interaction between Spin and Vibration in Molecular Junctions by Scanning Tunneling Microscope and High Resolution Spectroscopy

3.1 Abstract

The interaction between electron and vibration, i.e., vibronic coupling, in molecular junctions with scanning tunneling microscope (STM) has been under research for years. However few investigation on the coupling between vibronic and the spin degree of freedom has been performed using STM. We studied the possible interplay of the vibronic coupling to the spin dimension using two identical molecules, namely, Copper Phthalocyanine (CuPc) and Cobalt Phthalocyanine (CoPc). We observed both spin-vibronic progressions and spin-flip IETS over CoPc, while only spin-vibronic progression was observed on CuPc. Monotonic variation of the relative intensities of the spin-vibronic doublets as a function of the vibronic peak sequence number was observed with both molecules. The high resolved spectra observed under 600 mK provides more insight to the mechanism of electron tunneling through single molecule junction.

3.2 Article

Vibrational effect in molecule mediated electron transport has been of continuous research interest as it may lead to nano-electronics failure due to vibration induced dissociation, desorption and local heating effects. [1] However, additional influence resulting from the spin degree of freedom has been lack of investigation owing to complexities in experimental design including the needs of spin isolation, ultra-low temperature and high magnetic field. Besides, a macroscopic phenomenon, namely the Magnetostrictive effect and its reverse effect, the Magnetoelastic effect, motivate this study in that they describe the interplay between the change of magnetic property of material and the corresponding variation of the mechanical property of the material. [2] On the other hand, the microscopic picture of how single spin and vibration interact in a molecular junction is interesting and might help understand these effects. In principle an experimental setup with single molecular junction employing weak electronic couplings between the molecule and two electrodes may witness prominent spin effect under strong enough magnetic field. The STM setup with molecular tunneling junction, which leverages the highest spatial resolution capability, however only guarantees a weak electronic coupling Γ_t between tip and molecule, while the coupling between the molecule and substrate Γ_s is usually very strong. Interestingly, such concern has been investigated and resolved in early years when researchers were studying single spin-flip IETS, they inserted a ultrathin oxide layer (~5 Å thickness) between the adsorbed molecule and metal

substrate, hence reducing the electronic couplings Γ_s while still maintaining a strong enough conduction for electron tunneling. [3] This technique was quickly adopted later in an STM investigation of single molecular electron-vibration coupling where the vibronic signature was revealed. [4–8] The success of these experiments employing the oxide layer soon raised a new question: what will happen when the spin and vibronic effects are simultaneously excited? A more recent exploration using this technique answered this question and successfully resolved spin-vibronic progression for MgP molecules in neutral and affinity states. [9]

With the sub-Kelvin temperature of 600 mK and high external magnetic field up to ±9 Tesla, here we once again addressed the issue on spin-vibronic coupling by investigating two transition metal phthalocyanines, namely Copper Phthalocyanine (CuPc) and Cobalt Phthalocyanine (CoPc), where both may carry a single spin upon adsorption on oxide layers. The goal is to study the interaction between spin and the vibration of the molecule through spin-flip IETS and spin-vibronic progression. We found that although only CoPc shows spin-flip IETS signature at the center of the molecule, there is no evident difference in the spin-vibronic feature between these two molecules. And for both molecules, a monotonic variation of the relative intensities for the spin-vibronic doublets with respect to the vibronic sequence number is observed. This study provides more insights into the mechanism of electron tunneling through molecular junctions with spin-vibronic interactions.

The experiment was carried out on a home-built Helium-3 single-shot STM with lowest temperature at ~600 mK and capability of applying magnetic field perpendicular to the sample surface up to ±9 Tesla. CuPc and CoPc were deposited onto the partially oxidized NiAl(110) surface by thermal evaporation at about 28 K, respectively. The Ag tip was occasionally brought into contact with the metal surface for conditioning and sharpening. Spectra were taken with the tip positioning over different positions with feedback turned off. Spin-flip IETS manifests itself as steps in dI/dV, while spin-vibronic signatures, which correspond to resonant tunneling into real molecular states, display as peaks in dI/dV. The experiment was performed with magnetic field being at either +9 Tesla or -9 Tesla, no distinct difference between these two situations were observed.

Figure 3.1 a shows a typical dI/dV spectrum for a CuPc adsorbed on aluminum oxide surface and the inset is the topography of the molecule. With set bias of 1.5 V and set current of 0.1 nA, the spectrum range from -2.0 V to 1.5 V is where HOMO and LUMO of CuPc/Oxide usually locate. Due to the nature of double-barrier tunneling junction (DBTJ), the position of HOMO and LUMO will change with the tuning of tunneling set-point, that is, they both downshift to the Fermi level as the vacuum gap reduces. [4] For the CuPc we studied here, only the LUMO centered at ~0.8 eV is revealed. The sharp peak at ~-1.1 eV is the mirroring feature of the first vibronic peak at the onset of LUMO above the Fermi level, which is again a distinct signature of DBTJ. Although this spectrum is taken

with the tip positioning over the spot labeled by a circle, we believe it looks the same for spectrum taken at the spot labeled by a square.

With the tip positioning again over the spot labeled by the square, zooming into the onset of LUMO reveals interesting feature showing a series of dI/dV peaks (Figure 3.1 b). Because of the smaller tunneling gap set at 0.3 V and 0.3 nA, this onset appears closer towards the Fermi level than that in Figure 3.1 a. This finer spectrum reveals the first four vibronic peaks while those even higher order peaks are not resolvable possibly due to noise. The first two vibronic peaks split again with a spacing of ~ 1.4 meV due to the external 9 Tesla magnetic field which we assign to the spin-vibronic coupling. As for the 3rd and 4th vibronic peaks, however we cannot resolve the splitting, probably again due to noise. A spectrum analysis shows that the Gaussian fitting is not possible without a non-zero baseline. So each peak is fitted using a Gaussian function for approximation after the baseline being subtracted. The 3rd and 4th vibronic peaks are approximated with single broader Gaussian functions respectively due to the difficulty in resolving the Zeeman splitting. The peak positions are plotted against the peak numbers, following by a linear regression fitting. The first two data points are calculated by averaging the two corresponding spin-vibronic doublets positions, respectively. A nominal vibration energy of 4.0 meV can be deduced from the slope of the linear fitting, which we attributed to the skeletal doming mode of CuPc. [10] Considering the 15% correction due to the nature of DBTJ, we find the revised vibration energy is about $4.0 \times 85\% = 3.4$ meV and the

assignment remains valid since no other modes are nearby in energy and a 1 meV difference is within expectation when compared with the theoretical value derived from isolated molecules. If we assume that the Zeeman splitting at a zero external magnetic field is zero, then the Landé g factor calculated from the formula $\Delta_{eff} = g \mu_B B$ is 2.88 for the first vibronic peak and 2.50 for the second vibronic peak. By taking the nature of DBTJ into consideration, the corrected estimation for the g factor is 2.45 and 2.12 respectively. [9] Furthermore, we noticed the relative intensities for the spin-vibronic doublets varies as a function of vibronic peak number, so the reason for the difficulty in resolving the Zeeman splitting for the third and fourth vibronic might be due to that one peak dominates the other one.

Figure 3.1: STM dI/dV spectroscopy and the spin-vibronic progression for CuPc molecule adsorbed on aluminum oxide taken with bare Ag tip. (a) A typical dI/dV spectroscopy taken at the spot labeled with a circle over the molecule shown in the inset. It reveals a LUMO at around 0.8 eV. The sharp peak at around -1.1 eV is caused by the double barrier tunneling junction configuration. The spectrum is taken with a set-point of 1.5 V/0.1 nA and a bias modulation of 10 mV. The inset is a topographic image of CuPc on aluminum oxide taken with a set-point of 1.5 V/ 0.1 nA. The image size is 40 Å ×40 Å. A finer resolved dI/dV spectrum taken at the onset of the LUMO of the above molecule over the spot labeled by the square is shown in (b). The set-point used to take the spectrum is 0.3 V/ 0.3 nA and the bias modulation is 300 µV. The blue curve is fitted baseline with a second order polynomial fitting, which we assume it comes from the oxide background. Each peak is fitted with Gaussian function as shown by the green curves. The first and second vibronic peak show Zeeman splitting and thus are fitted into two Gaussian functions respectively. The third and fourth vibronic peak show only one peak and thus are fitted by one Gaussian function respectively. The sum of all the Gaussian curves yields the overall profile of the spin-vibronic progression as shown by the red curve. The inset shows the peak positions extracted from the vibronic progression. The linear regression reveals a slope of 4.0 meV. The first two data points are derived from the average of the first two spin-vibronic peaks respectively.
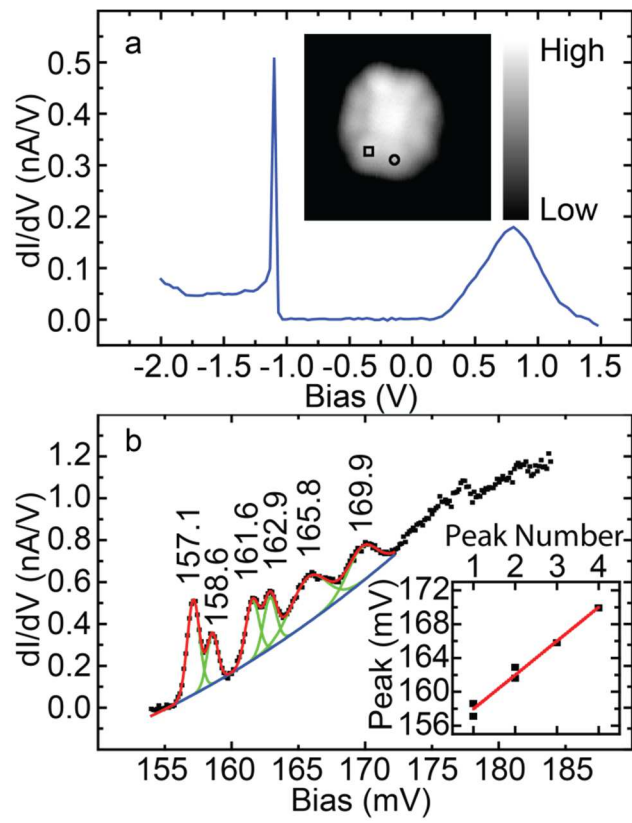
No evident spin-flip signal is observed from the IETS around the Fermi level taken over CuPc, under the external ±9 Tesla magnetic field. In contrast, with the same magnetic field, strong spin-flip IETS is revealed around the Fermi level for CoPc adsorbed on the oxide, indicating a remaining single spin. Figure 3.2 a shows the I-V and dI/dV spectra taken at the center of a CoPc shown in the inset of Figure 3.3 a, together with the d^2I/dV^2 spectrum in Figure 3.2 b. A Gaussian fitting of the d^2I/dV^2 spectrum reveals a spin-flip excitation at ~ 1 meV. The discrepancy between the absolute values of IETS peak and dip may result from the Stark effect, [11,12] however we also suspect that it might come from the instruments itself. Notice that this IETS threshold values does not change with the tuning of the tunneling gap, which is in contrast to how a spin-vibronic spacing varies under different tunneling set points.

Figure 3.2: Spin-flip IETS taken over the center of a CoPc molecule adsorbed on oxide. (a) I-V curve shown with blue triangles and dI/dV curve shown with black squares taken together with the spin-flip IETS. (b) d^2I/dV^2 spectrum for the spin-flip IETS. These three spectra are taken simultaneously with the bare tip positioning over the center of a CoPc molecule with a set-point of 0.1 nA/ 10 mV and bias modulation of 100 µV. The peak and tip in the spin flip IETS are fitted by Gaussian functions respectively shown by the green dashed curve. The red curve is the sum of these two Gaussian fitting curves.
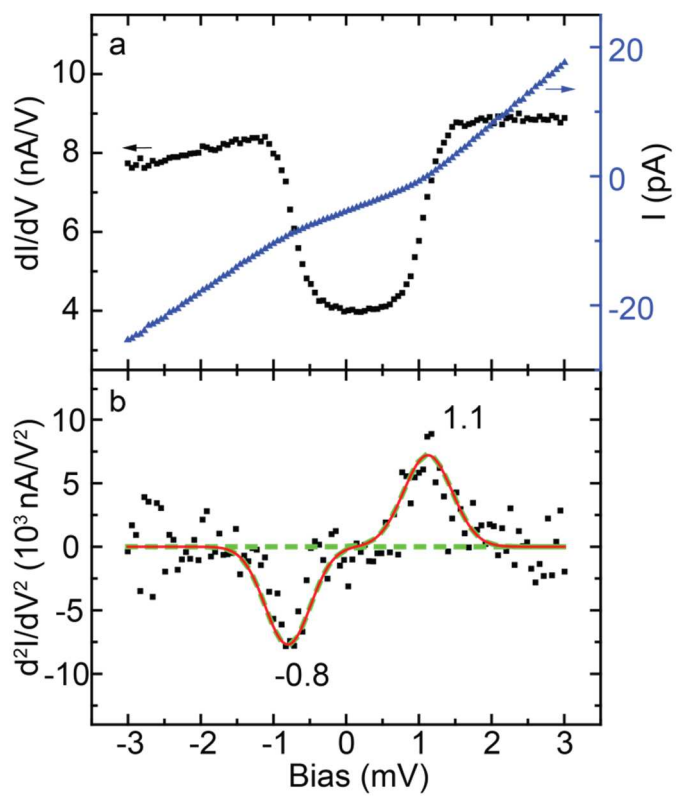
The vibronic progression of CoPc taken at the same position is shown in Figure 3.3 a and a total of 13 vibronic peaks are resolved. Plotting of the peak positions against peak numbers is shown in Figure 3.3 d, and it again fits to a straight line whose slope is the nominal vibration excitation energy. By taking the 15% correction into consideration, we obtain a revised vibration energy of about $3.3 \times 85\% = 2.8$ meV, which is again assigned to the skeletal doming mode of CoPc. Note that no conclusion can be drawn from the comparison of this vibrational energy to the same mode of CuPc, because the oxide thicknesses underneath these two particular molecules may be different. Figure 3.3 b shows a zoom-in dI/dV spectrum resolving the first three set of spin-vibronic peaks from the above vibronic progression. Again a non-zero baseline is needed for fitting. The spin-vibronic peaks are fitted with Gaussian function after a baseline being subtracted and the corresponding peaks positions are plotted against peak number shown in Figure 3.3 c, the nominal vibrational energy deduced from the slope from the two linear fittings are 3.1 meV and 3.2 meV respectively, which are quite closed to that in the aforementioned vibronic progression fitting. Note that the spectra in Figure 3.3 a and Figure 3.3 d are taken under different tunneling set-points and modulations, so the peaks positions and nominal vibration energies are slightly different. The Zeeman splitting of those even higher vibronic peaks is not resolvable and hence is not shown here. By assuming a zero splitting under zero magnetic fields and a 15% correction resulting from the DBTJ configuration, we reach estimations of the g factors of 1.96, 1.63 and 1.63 respectively. We are

uncertain with the value of the g factor because the exact value of voltage drop across the molecule is impossible to estimate from the experiments. We also notice a monotonic variation of the relative intensities of the spin-vibronic doublets as a function of the vibronic number. The first spin-vibronic peak grows in relative intensity as the peak number increases, which is in opposite to the case observed for CuPc. The exact mechanism behind this phenomenon is unknown but at least we can rule out a possible cause from the orientation of the external magnetic field. The reasoning is that if the direction of the external magnetic field matters, there must be a strong internal field of the same scale of ~ 1 Tesla already, but a spin-flip IETS has never been observed with a zero external field.

Figure 3.3: Spin-vibronic progression observed from a CoPc molecule adsorbed on oxide. (a) dI/dV vibronic progression taken at a set-point of 40 mV/ 0.1 nA with bare Ag tip positioning over the center of CoPc shown in the inset. The bias modulation used is 500 μV. The red curve is a guide for the eyes connecting all the points. The inset shows the topographic image of the CoPc taken with a set-point of 1V / 0.1 nA. The size of the image is 30 Å × 30 Å. A zoomed-in dI/dV spectrum showing the finer detail of the first three vibronic peaks is shown in (b). The set-point is 60 mV/ 0.1 nA and the bias modulation is 100 μV. A 5th order polynomial curve is used for the baseline shown in blue, which we assume it comes from the oxide background. Then each peak is fitted using a Gaussian function indicated by the green curves and the red curve is the sum of all the individual fittings. The vibronic peak position vs. peak number extracted from (a) is shown in (c). A linear regression fitting reveals a slope of 3.3 meV. The spin-vibronic peak positions vs. peak numbers extracted from (b) is shown in (d). As each vibronic peak splits into two spin-vibronic peaks, two linear regressions are individually fitted to the 1st and 2nd spin-vibronic peaks derived from each vibronic peak. The fittings yield slopes of 3.1 meV and 3.2 meV respectively.

a

37.6
39.3
43.6
47.0
50.1
53.7
57.1
60.3
63.6
66.9
70.4
73.4
76.7

dI/dV (nA/V)

60
50
40
30
20
10
0

High

Low

Bias (mV)
30   40   50   60   70   80

b

42.2
43.4
45.5
46.5
48.6
49.6

dI/dV (nA/V)

12
10
8
6
4
2
0

Bias (mV)
42   44   46   48   50

c

Peak (mV)

80
70
60
50
40

Peak Number
1   5   9   13

d

Peak (mV)

50
48
46
44
42

Peak Number
1   2   3
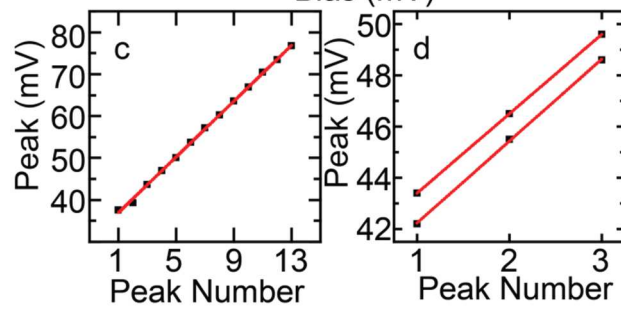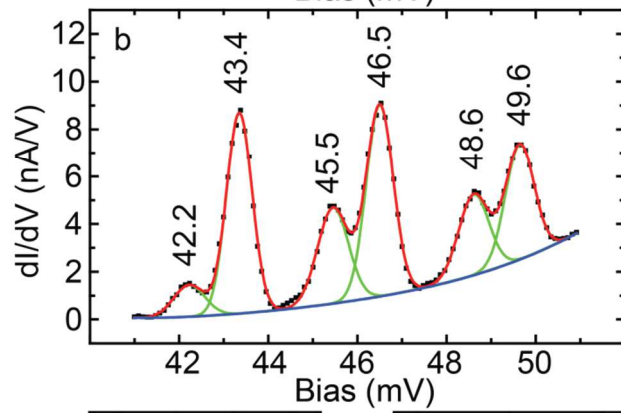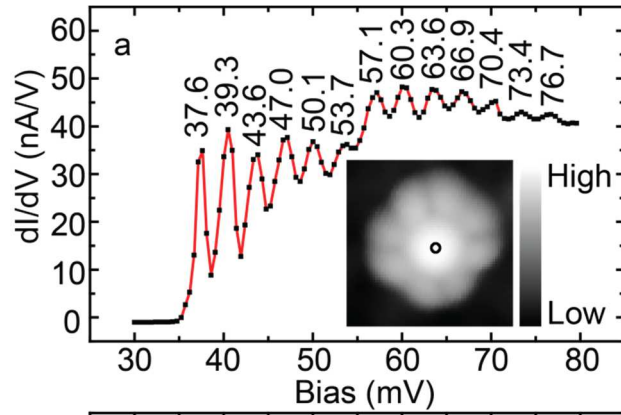
A proposed schematic diagram for the tunneling mechanism with spin-vibronic coupling is shown in Figure 3.4. The regular vibronic interaction manifests itself as electronic states progression on top of the molecular LUMO, and the spin-vibronic interaction further splits each vibronic state into a spin up state and a spin down state when an external magnetic field presents. The electrons from the tip resonantly tunnels into these levels, depicting the profile of spin-vibronic progressions. Similarly, when electron tunnels from substrate under a reversed bias polarity, the dI/dV spectrum also reveals progressions, but with larger spacing between vibronic peaks and larger Zeeman splitting. During the tunneling process, the molecules are believed to stay in a transient negative charged state. [8]

Figure 3.4: Schematic diagram illustrating the mechanism for electron tunneling through the spin-vibronic states. The molecule is sandwiched between the oxide and the vacuum gap in a double barrier tunnel junction connected to the Ag tip and NiAl(110) substrate. Under an external magnetic field, each vibronic state splits into spin-vibronic doublets. As the sample bias is swept and aligned with each state, resonant tunneling occurs thus the dI/dV depicts the profile of spin-vibronic progression. The molecule is in a transient charged state during the electron tunneling process.
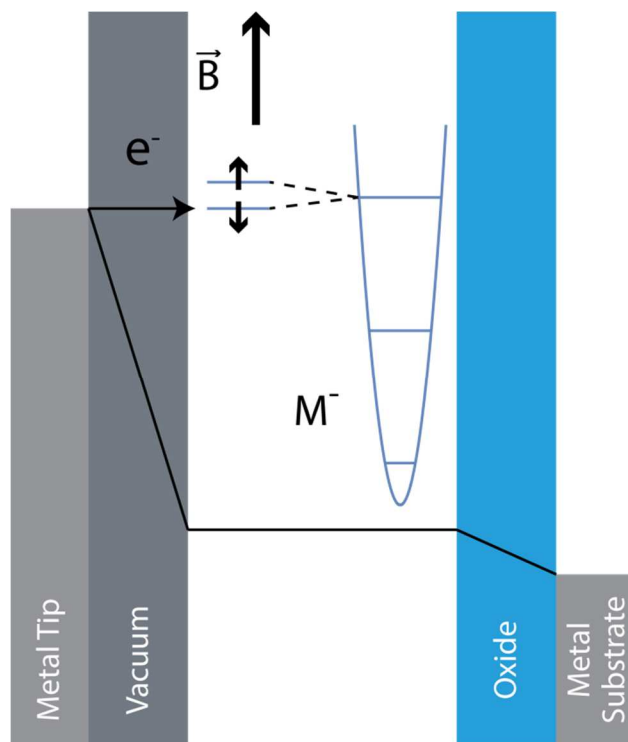
In summary, we revisited the interaction between spin and vibration, i.e., spin-vibronic coupling with two identical molecular systems, namely CuPc and CoPc adsorbed on aluminum oxide using STM. CoPc retains a single spin by exhibiting spin-flip IETS signature around the Fermi level, while no such feature was observed on CuPc molecule. Meanwhile both molecules show similar spin-vibronic progressions at the onset of LUMO, respectively. The vibration energies derived from the linear fitting of both the vibronic progressions of these two molecules are assigned to the skeletal doming motion of metal phthalocyanine molecules. The Landé g factors obtained are also closed to the value of previous results. A monotonic variation of the relative intensities for the spin-vibronic doublets is observed for both CuPc and CoPc. This study of the interaction between spin and vibration of metal phthalocyanine molecules using sub-Kelvin STM provides deeper understanding to the mechanism for electron tunneling through molecular junctions.

3.3 Bibliography

[1]   K. Franke and J. Pascual, Journal of Physics: Condensed Matter **24**, 394002 (2012).

[2]   H. Meyers, *Introductory Solid State Physics* (1997).

[3]   A. J. Heinrich, J. A. Gupta, C. Lutz and D. Eigler, Science **2004**, 466–469 (2004).

[4]   X. Qiu, G. Nazin, and W. Ho, Physical Review Letters **92**, 206102 (2004).

[5]   Q. Huan, Y. Jiang, Y. Zhang, U. Ham, and W. Ho, Journal of Chemical Physics **135**, 014705 (2011).

[6]   H. Lee, J. Lee, and W. Ho, ChemPhysChem **6**, 971 (2005).

[7]   N. Liu, N. Pradhan, and W. Ho, Journal of Chemical Physics **120**, 11371 (2004).

[8]   N. Ogawa, G. Mikaelian, and W. Ho, Physical Review Letters **98**, 166103 (2007).

[9]   U. Ham and W. Ho, Physical Review Letters **108**, 106803 (2012).

[10] Liu, L.; Dienel, T.; Widmer, R.; Gröning, O. *ACS Nano* **9**, 10125–10132.(2015).

[11] L. Lauhon and W. Ho, Physical Review B **60**, R8525 (1999).

[12] L. Lauhon and W. Ho, Review of Scientific Instruments **72**, 216 (2001).

Chapter 4 : Imaging the Three Dimensional Variations of the Potential Energy Surface of Adsorbed Molecules

4.1 Abstract

The skeletal structure of single molecules has been imaged by the noncontact atomic force microscope (NC-AFM) and the inelastic tunneling probe with the scanning tunneling microscope (itProbe). To date, applications have been mainly confined to the study of cyclic molecules. Here we extend itProbe to investigate acyclic ethylene molecules adsorbed on Ag(110) surface and particularly reveal the three dimensional variations of the potential energy surface. In addition, itProbe imaging provides direct visualization of the changes in the potential energy surface associated with the formation of a dimer of trans-1,2-dichloroethylene on the surface.

4.2 Article

Recent advances in imaging by scanning probes have revealed molecular skeletal structures in single molecules and interactions between molecules, including but not limited to covalent and hydrogen bonds. [1−7] Although the validity of the 'hydrogen bonds' in the observed images has been debated, [8] the resolved structures provide new possibilities to understand the nature of the chemical bonds and intermolecular interactions. Imaging molecular structures have been realized by NC-AFM and itProbe by the STM. [2,5] In both techniques, the decoration of the probing tip with a single carbon monoxide (CO) molecule plays a crucial role in enhancing the resolution in order to reveal bonds. For the itProbe, the various contrasts and features in the images can be correlated with the ridges and saddle points in the potential energy surface that the CO molecule senses as it scans over the molecule. [5,9]

To date, only cyclic molecules have been investigated, being either carbocyclic or heterocyclic compounds. [1−5,10,11] In order to extend the capability of the AFM and STM based structural imaging techniques, it is not only interesting but also necessary to examine an acyclic compound, such as ethylene (C_2H_4) which is expected to lay flat when it is adsorbed on the surface. [12−15]

In the present study, we investigated the structure of C_2H_4 using the itProbe technique. [5] We successfully imaged a structure which closely matches the known molecular structure. Direct measurements from the itProbe images

yield 1.4 ± 0.1Å for the C-C bond length and $110 \pm 2°$ for the H-C-H bond angle, which are in good agreement with the theoretical values of 1.339 Å and 117.4° for C_2H_4 in the gas phase. [16] For comparison, we also studied the trans-1,2-dichloroethylene adsorbed on Ag(110) substrate. The trans-1,2-dichloroethylene molecules are observed to form clusters when dosed onto Ag(110) at 25 K. For simplicity and clarity, the current study focused on dimers. In contrast to the symmetric structure that was imaged for the C_2H_4 molecule, the trans-1,2-dichloroethylene dimers show asymmetric structure that is consistent with the asymmetry in the molecule.

The experiments were carried out on a home-made STM at a temperature of 600 mK and base pressure of 5.0×10^{-11} Torr. [17] We studied the regular C_2H_4 and the trans-1,2-dichloroethylene molecules in two separate experiments. The Ag(110) is chosen as the substrate for its exceptional atomic flat surface. Both the Ag tip and substrate were repeatedly sputtered and annealed several times during the preparation stage. The C_2H_4 and the trans-1,2-dichloroethylene went through several degassing cycles of freeze-pump-thaw before being introduced to the system. The CO molecules were dosed onto the substrate to a coverage of ~0.05 monolayer after the deposition of C_2H_4/ trans-1,2-dichloroethylene. The temperature of the substrate was at 25K during the depositions of these molecules. [5]

As what we have already demonstrated in a previous study, the CO decorated on the tip is the key for the STM itProbe imaging and the enhanced

topographic resolution. [5] A CO-tip is usually obtained after a near-surface scanning, typically with a set-point of 1 mV/1 nA, over a CO with a bare Ag tip. The CO molecule reacts to the potential curvature variation introduced by the underlying molecule on surface, hence producing a shift to the hindered translational mode in the IETS. By recording the d^2I/dV^2 signal at a certain probing sample bias, the itProbe image turned out to resemble closely the bonding structure of the molecule on surface. [5,9]

In Figure 4.1 we show a series of IETS which were taken with the CO-tip positioned over C_2H_4 at different locations. Because the itProbe image in a constant-height mode yields better results, the procedure for taking these spectra follows the same protocol as the one in our previous report, i.e., the feedback is turned off over the center of the molecule, and the spectra are taken after the tip subsequently moves to those 10 different positions, followed by tip advancement in z direction. [5] Topographic images were taken in-between these spectra to ensure minimal lateral drift. Except for the one taken on the background, each spectrum reveals two vibrational IETS signatures within the 10 meV range around the Fermi level. The one with lower vibrational energy around 1.5 meV corresponds to the hindered translational mode of the CO molecule on tip. We observe that C_2H_4 shows no IETS feature in this range, so we believe that when the CO tip moves closer to the C_2H_4, the degeneration of the hindered translational mode will be lifted, hence this mode is again a CO hindered translational mode which is perpendicular to the one above.

Figure 4.1: Point spectroscopy taken with a CO-terminated tip in the constant-height mode at different locations over a single C_2H_4 molecule adsorbed on Ag(110) surface as shown in the schematic of the molecular structure. The detailed procedure for taking these spectra is described in the main text. Ten spectra by inelastic electron tunneling spectroscopy with the STM (STM-IETS) are recorded and offset for clarity. Spectra from 1 to 9 reveal vibrational features in the range 1.3-1.8 mV and 6.0-6.7 mV. The spectrum over the Ag background only has one vibrational signal corresponding to the hindered translational energy at 2.5 meV for the CO molecule on tip. Thin horizontal lines indicate the zero baselines for each spectrum. The two dot-dash vertical lines indicate the sample bias of 1.5 mV for recording the itProbe images.
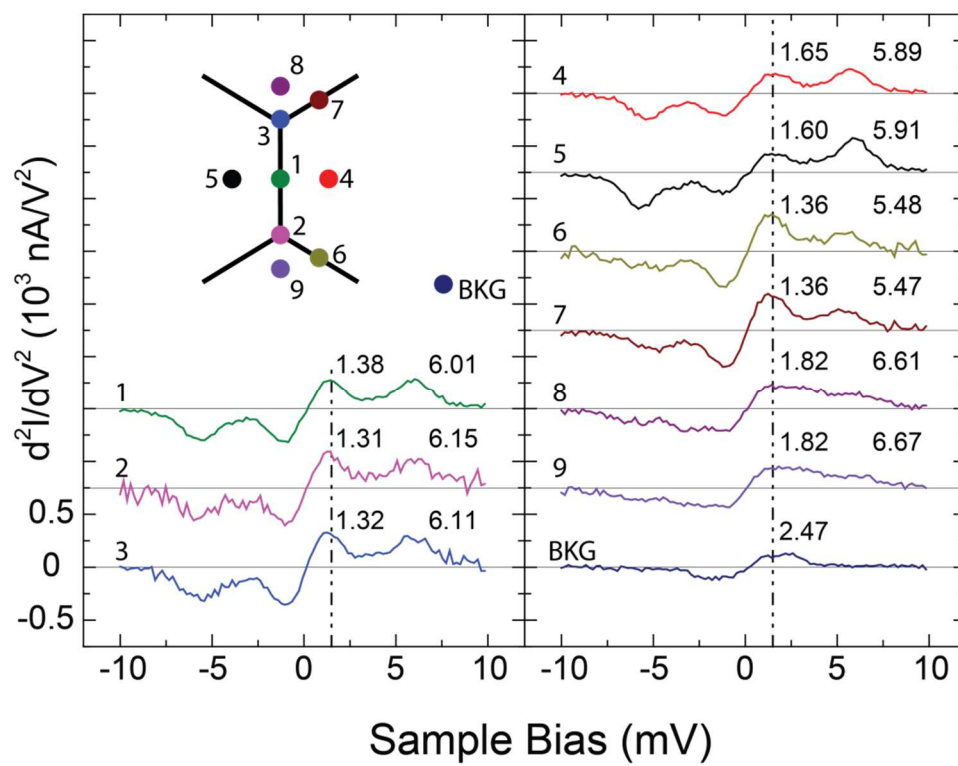
A constant-height mode itProbe image is shown in Figure 4.2c. The imaging procedure is the same as the one we described in the previous study, [5] with the initial feedback turned off over the center of C_2H_4. It was demonstrated that an itProbe image is sensitive to the tip-sample separation and the probing sample bias. [5] The one in Figure 4.2 is selected due to the high contrast and the clear bonding structure it reveals. From the high-resolution topographic image in Figure 4.2b we can determine the adsorption site for the C_2H_4 molecule. It turns out the C_2H_4 molecule prefers to adsorb on an atop site on Ag(110) surface. The schematic diagram is displayed in Figure 4.2a. The C-C bond length we derived from this schematics is equal to 1.4 ± 0.1Å and the bond angle of H-C-H is $110 \pm 2°$, which are in agreement with the theoretical values of 1.339 Å and $117.4°$ for a C_2H_4 molecule in the gas phase. [16] We attribute the H-C-H bond angle discrepancy to the fact that each C-H bond may not be parallel to the Ag(110) surface. [18]

Figure 4.2: Images recorded in the constant-height mode for an isolated C_2H_4 molecule adsorbed on Ag(110). (A) Schematic diagram of a model for the molecule adsorbed on an atop site of Ag(110) surface. The carbon atoms and C-C bond are colored in black and the C-H bonds are colored in black and blue. (B) Image of the Ag(110) surface atomically resolved with the CO-tip and the STM junction set with sample bias of 10 mV and tunneling current of 0.5 nA. The white dots indicate the atop-locations of the Ag atoms, enabling the extraction of the adsorption site for the C_2H_4 molecule. (C) The constant-height itProbe image for C_2H_4 on Ag(110). The itProbe image is taken with a tip-sample gap of 2 Å smaller than the junction set at 0.1 V/ 0.1 nA with the CO-tip positioned over the center of C_2H_4. (D) The same itProbe image as (C) with the stick model of C_2H_4 overlaid on top. (E) *dI/dV* image and (F) current image, recorded simultaneously at the same junction gap as the itProbe image. (G) Current image recorded at the junction gap set at 0.1 V/0.1 nA. (H) Topographical z-image recorded simultaneously at the same junction gap as the itProbe image. Except for the 32 Å x 32 Å size in (B), all other images have dimensions of 9 Å x 9 Å.
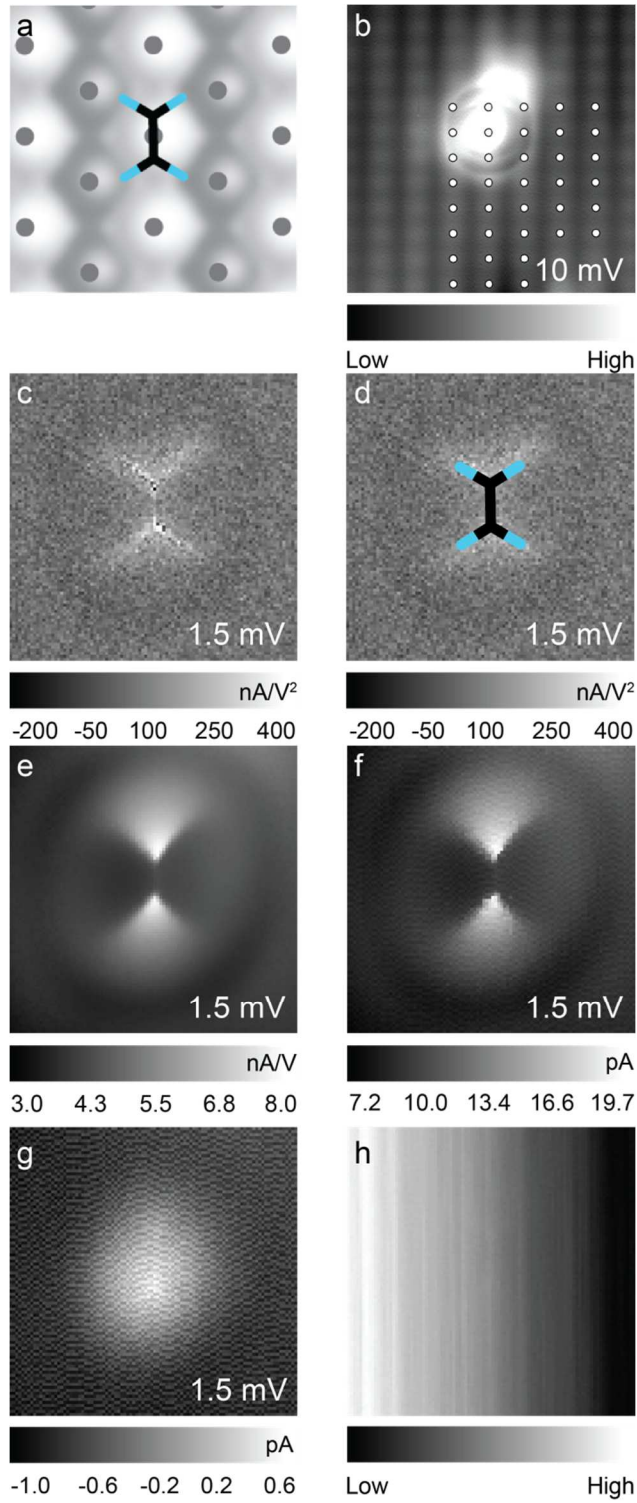
It is interesting to survey the dependency of the itProbe image as a function of the tip-sample separation since we believe the itProbe images will provide a direct visualization of the three dimensional variations of the potential energy surface. In Figure 4.3 we show a sequence of itProbe images by tuning the gap from $\Delta z = 1$ Å to $\Delta z = 2.6$ Å with a step of about 0.33 Å, all at a probing sample bias of 1.5 mV. As it is expected, the one at $\Delta z = 2.0$ Å gives the most prominent image that resembles the bonding structure of a single C_2H_4 molecule. The $\Delta z = 0$ is a tentatively defined reference tunneling gap with a set point of 0.1 V/ 0.1 nA with the CO-tip positioned over the center of the C_2H_4 molecule. The Δz is set in a way that the tunneling gap becomes smaller when it increases. This series of images shows an interesting pattern such that as the tip moves closer to the molecule, the imaged bonding structure changes from a single oval shape to the best resolved structure with a clear defined C-C bond, and finally to an even larger skeleton structure with a blurring C-C bond when the tip-sample separation is as close as $\Delta z = 2.6$ Å. We attribute the change in these itProbe images to the variations of the potential energy surface as a function of height. When the tip is far away from the C_2H_4 molecule on the surface, the influence due to the C_2H_4 molecule onto the hindered translational motion of the CO molecule is weak, thus only the center part of the itProbe image is bright. When it reaches $\Delta z = 2.0$ Å, the interactions between CO and the bonds of C_2H_4 become strong, hence a clear bonding structure of the C_2H_4 is revealed. [19] As the tip moves even closer to C_2H_4 molecule, the deeper part of the potential energy surface is revealed. Note

however that we could not rule out the possibility that the CO on the tip apex might tilt to some extent when the tunneling gap is too small, [8] we believe the influence from the potential energy surface dominates the contrast of the itProbe images. The complete sets of constant height itProbe images with varying Δz, including dI/dV image, current images and z-image, are all shown in Figure 4.4. These images are arranged from the left to the right in the order of: d^2I/dV^2 itProbe image at 1.5 mV after tip advancement, dI/dV image at 1.5 mV after tip advancement, current image at 1.5 mV after tip advancement, current image at 1.5 mV at $\Delta z = 0$ and z-image at 1.5 mV after tip advancement. The z-images are recorded to evidence a constant height during the time of imaging. The coloring gradient is resulted from the subtle piezo drift in the direction perpendicular to the Ag(110) surface.

Figure 4.3: Constant-height itProbe images for different tunneling gaps. Details of the procedure for constant-height itProbe imaging are described in the main text. All images are recorded at sample bias = 1.5 mV. $\Delta z = 0$ is defined as the tunneling gap when the tip is parked over the center of C_2H_4 with set-point of 0.1 V/ 0.1 nA. As Δz increases the tip-molecule gap decreases. The size of each image is 9 Å x 9 Å. The complete set of images associated with each itProbe image, including *dI/dV*, current, and topography, are shown in Figure 4.4.
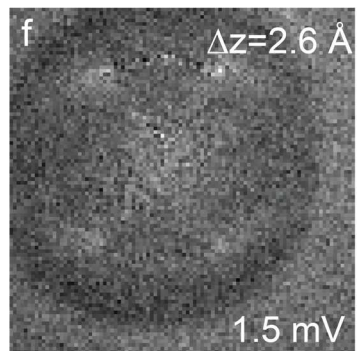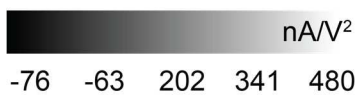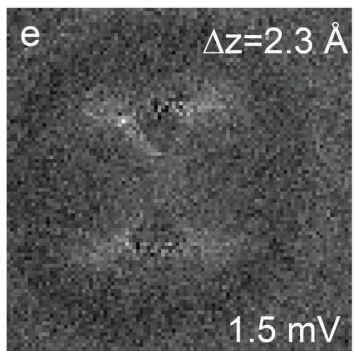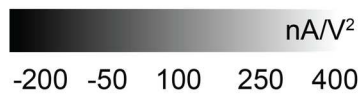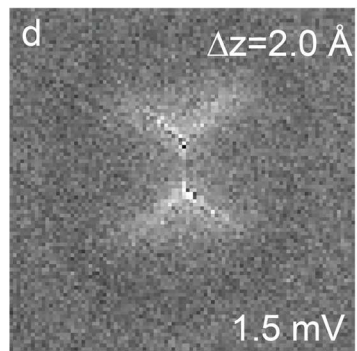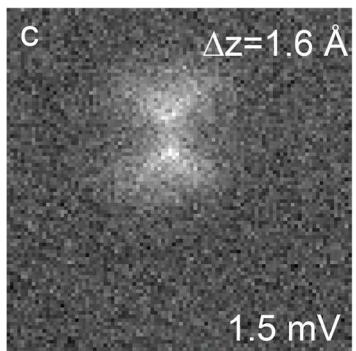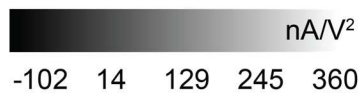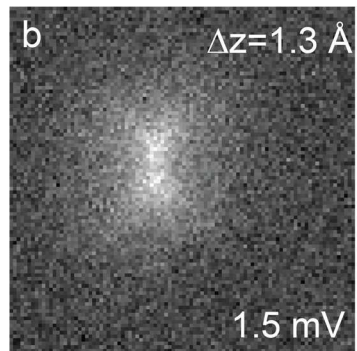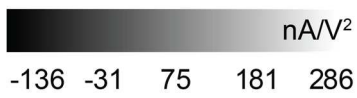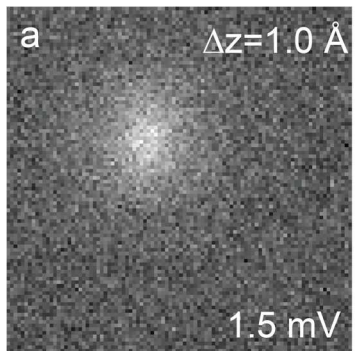
Figure 4.4: Constant-height images with varying Δz, all at sample bias of 1.5 mV. $\Delta z = 0$ is defined as when the CO-tip is parked over the center of C_2H_4 with a set-point of 0.1 V/ 0.1 nA. The gaps being surveyed range from a decrease of $\Delta z = 1.0$ Å to $\Delta z = 2.6$ Å. The images in each row are arranged from left to right in the order of d^2I/dV^2 itProbe, dI/dV, current, current image at $\Delta z = 0$, and topography. All images are recorded after Δz change, except for the current image taken at $\Delta z = 0$.
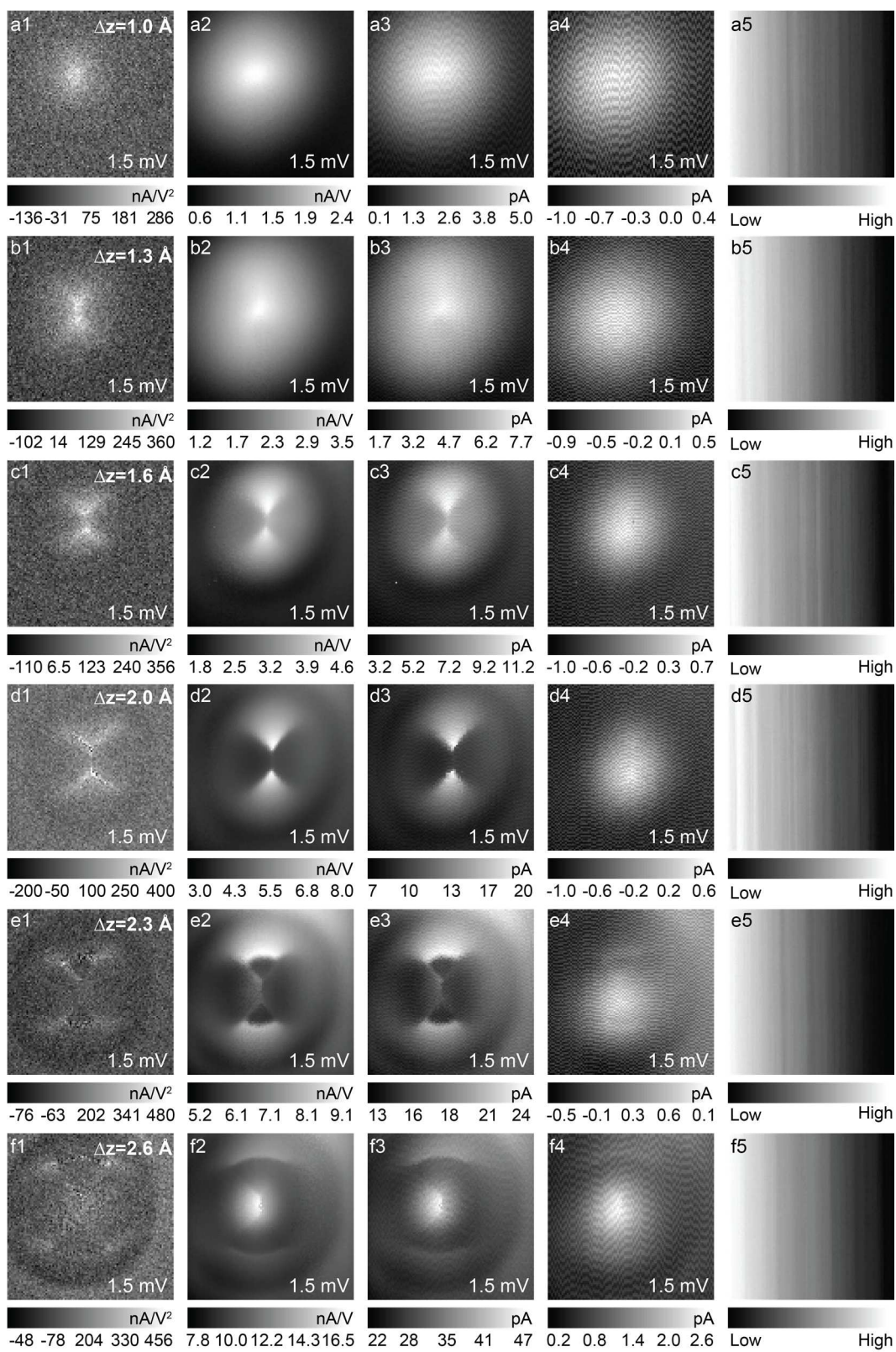
There is an additional degree of freedom for STM itProbe imaging in constant height mode, which is known as the probing sample bias. A sequence of itProbe images are displayed in Figure 4.5 with different probing biases ranging from 1.0 mV to 18.5 mV, all at the tunneling gap taken at $\Delta z = 2.0$ Å. The probing sample biases from 1.0 mV to 1.75 mV are chosen for their proximity to the hindered translation energy of the CO molecule, and the one at 5.0 mV is selected because of the other hindered translational energy of CO nearby. And finally the one at 18.5 mV is surveyed for its closeness to the hindered rotation energy of CO molecule. One can easily observe bonding structures in the images from Figure 4.5a to Figure 4.5d, while it is hard to tell one in Figure 4.5e and the image is too noisy in Figure 4.5f. We believe the image in Figure 4.5e is related to the higher energy hindered translational mode of CO due to the lift of degeneration. We ascribe the noise in Figure 4.5f to the induced motion of CO molecule when the tip is positioning over the bonds and atoms. By scanning through different bias range with a fixed tunneling gap, we can survey the potential energy surface influence on different energy of the CO molecule. The negative curvature induced by this potential energy exert more influence on the soft low energy modes of the CO, while it has minimum to zero effect on the shifting of high energy modes of CO, thus the itProbe image at 18.5 mV shows barely any contrast. The complete sets of images taken together with each itProbe image in Figure 4.5 are shown in Figure 4.6. These images are arranged from the left to the right in the order of: d^2I/dV^2 itProbe image after tip advancement,

dI/dV image after tip advancement, current image after tip advancement, current image at $\Delta z = 0$ and z-image after tip advancement, all with the probing bias set beforehand. The z-images are recorded as an evidence for gap stabilization.

Figure 4.5: Constant-height itProbe images for different sample biases. Details of the procedure for constant-height imaging are described in the main text. $\Delta z = 0$ is defined as the tunneling gap when the tip is parked over the center of C_2H_4 with set-point of 0.1 V/ 0.1 nA. All itProbe images are taken with the tip-molecule gap set at $\Delta z = 2$ Å. The size of each image is 9 Å x 9 Å. The complete set of images associated with each itProbe image, including dI/dV, current, and topography, are shown in Figure 4.6.
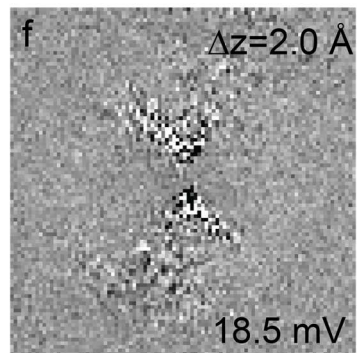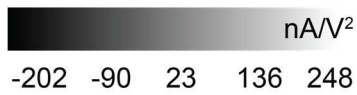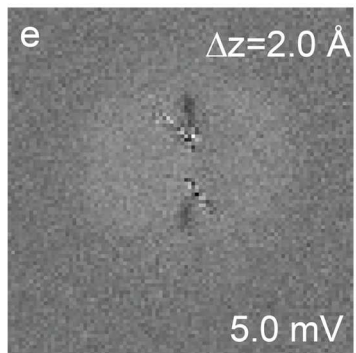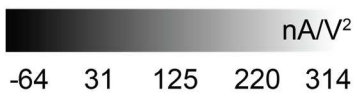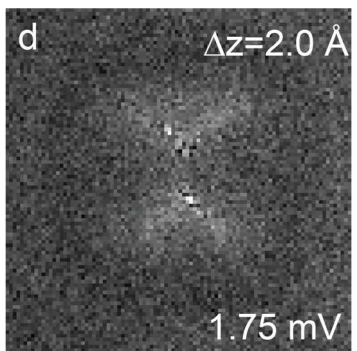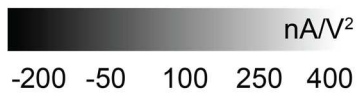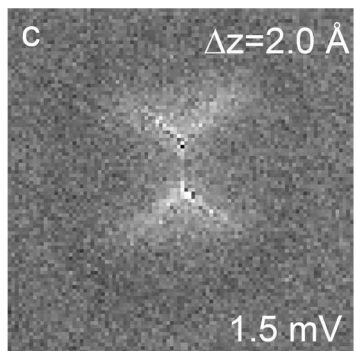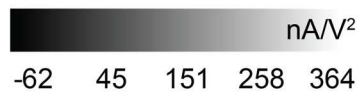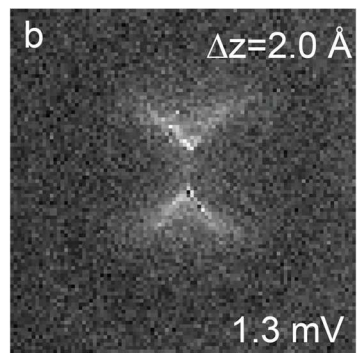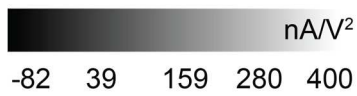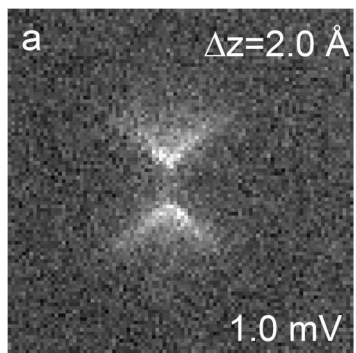
Figure 4.6: Constant-height images recorded at different sample biases, all at a fixed $\Delta z = 2.0$ Å from the set-point of 0.1 V/0.1 nA. The probing sample biases range from 1.0 mV to 18.5 mV. These images in each row are arranged from the left to the right in the order of: d^2I/dV^2 itProbe, dI/dV, current, current image at $\Delta z = 0$, and topography. All images are recorded after Δz change, except for the current image taken at $\Delta z = 0$.
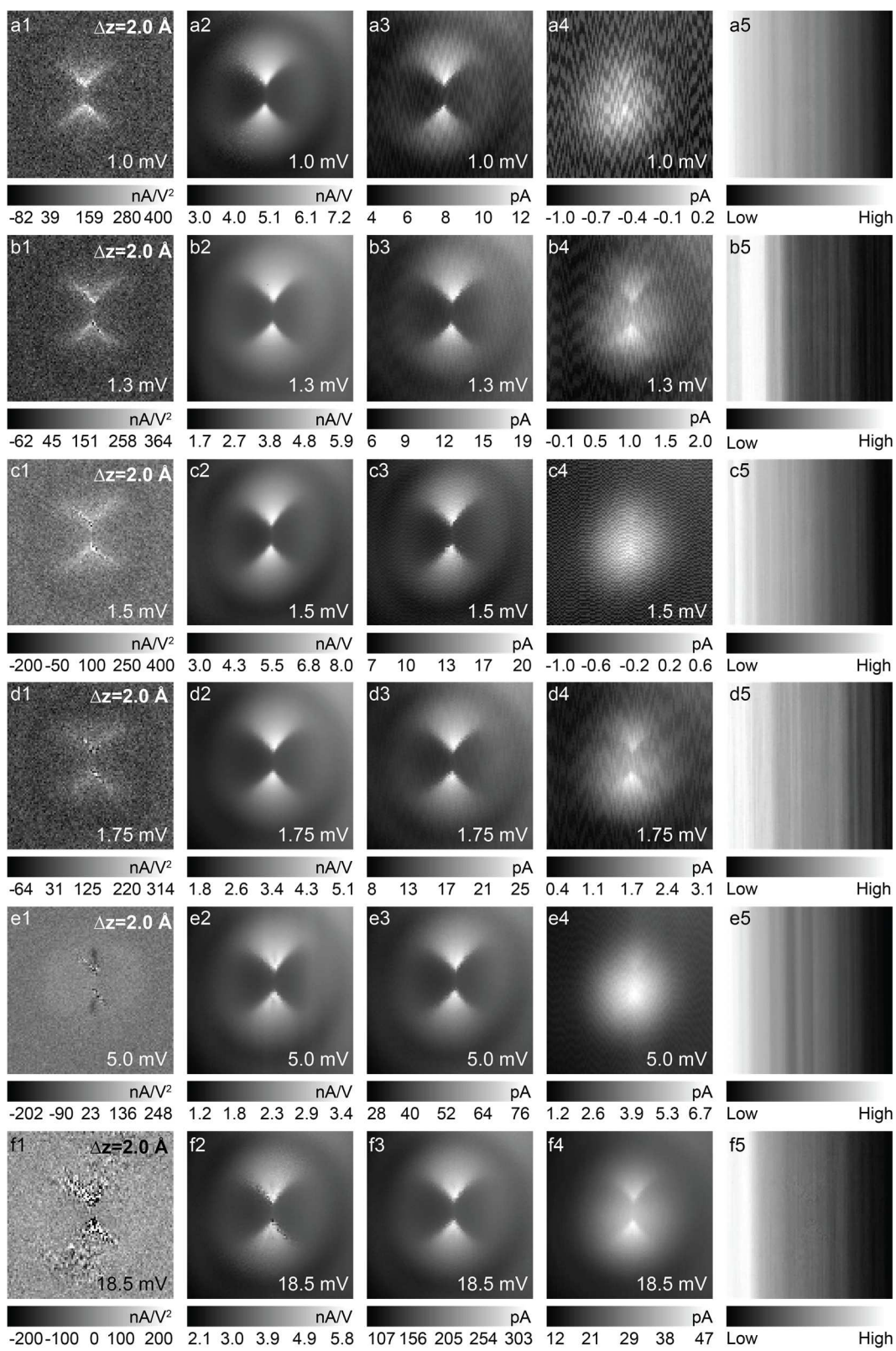
For comparison, we further investigated the trans-$C_2H_2Cl_2$ molecule. We were not able to find an isolated trans-$C_2H_2Cl_2$ molecule on Ag(110) surface, so we chose a dimer to focus on for simplicity. To better visualize the inter-molecular bonding structure, we took the itProbe image using the constant current mode, together with a comprehensive survey of the d^2I/dV^2 spectra taken over different locations. They are all with a set-point of 15 mV/0.1 nA and are shown in Figure 4.7. The reason for the proposed schematic diagram is discussed below. We tentatively categorize the spectra into groups using different colors. Spectra with the same color are those taken over spatially similar locations, e.g., the spectra for the two C-C bonds are colored in black and the spectra over those C-Cl bonds are colored in dark green etc. A preliminary analysis suggests the spectra taken nearby a Chlorine atom (i.e., Cl_11, Cl_12, $\alpha1$, $\alpha2$, $\alpha3$, β, δ and ξ) all have two vibrational modes revealed, one at ~ 1.5 mV and the other one at ~ 4 mV. Again, we ascribe this to the lift of modes degeneration due to the closeness of CO-tip to the dimer. And those taken closed to Carbon atoms (i.e., H, C-C and C-Cl bonds) only show a single peak ranging from 1.1 mV to 2.0 mV.

Figure 4.7: Point spectroscopy taken with a CO-terminated tip in the constant-current mode for a trans-$C_2H_2Cl_2$ dimer on Ag(110) surface. All spectra are recorded with the tunneling gap set at 15 mV/0.1 nA. A total of 22 IETS spectra are recorded and offset for clarity. Spectra taken over similar spatial positions are grouped together and indicated by the same color. Thin horizontal bars in each spectrum indicate the zero base line. The vertical dot-dash lines indicate the sample bias selected for the constant-current itProbe imaging. 12 of 22 spectra are magnified by a factor of 2 to better reveal the vibrational signatures. A schematic diagram of the dimer is extracted from the itProbe image. The carbon atoms and C-C bonds are colored in black; the C-H bonds are colored in black and blue; the C-Cl bonds are colored in black and green. Dashed lines are drawn to indicate the interactions between the two trans-$C_2H_2Cl_2$ and their interactions with the substrate. Filled circles indicate the locations where some of the spectra are recorded, while other spectra are taken either in the middle of the bonds or over the atoms in the molecules.
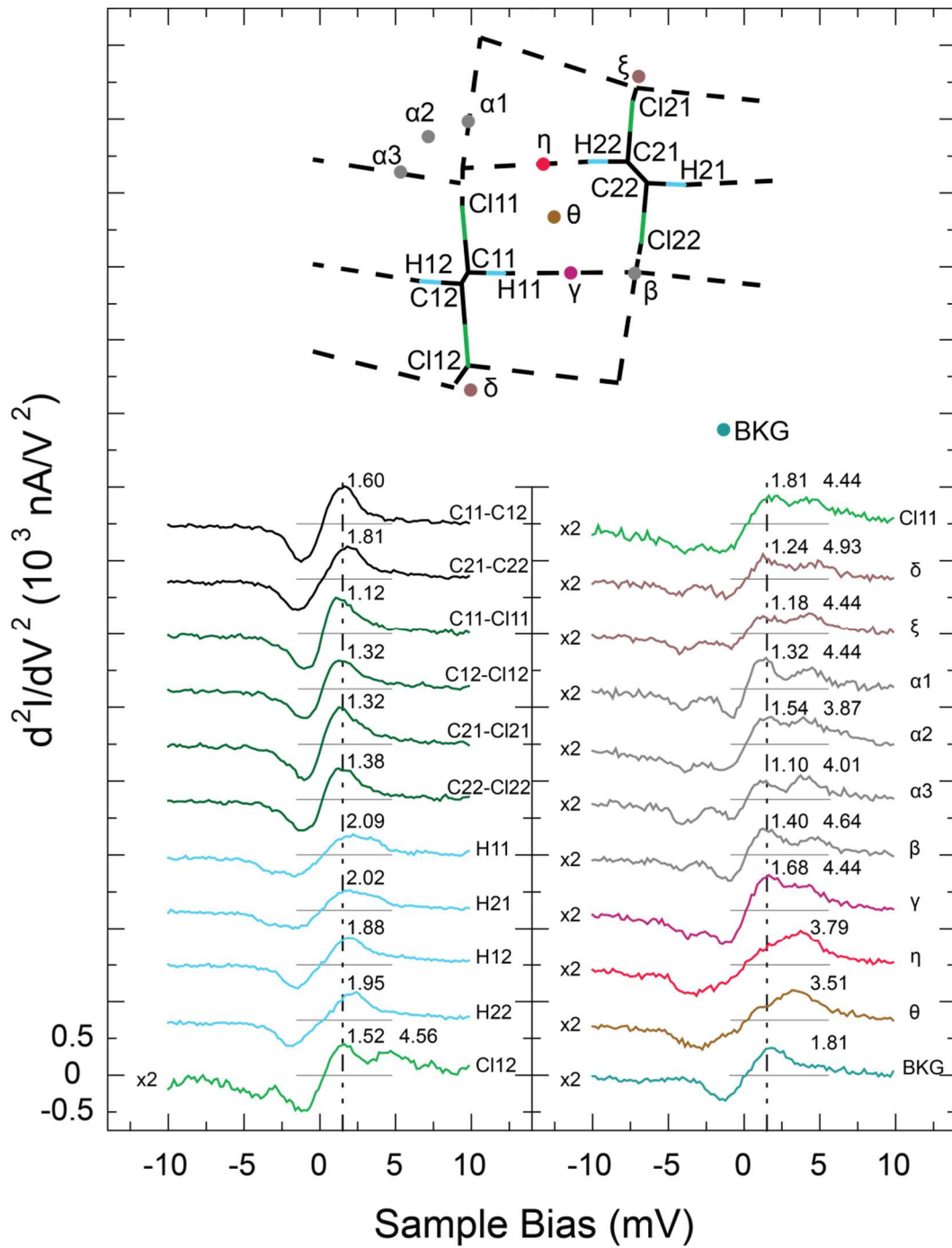
The constant current itProbe image of the trans-1,2-dichloroethylene dimer is displayed in Figure 4.8c. An apparent asymmetry is revealed for both of the molecules. The same image with an overlay of the schematic diagram is shown in Figure 4.8d. The model representation shows clear distortions and we believe it is resulted from the interaction with the substrate. The reason for the orientation assignment of the two molecules is as follows, compared to C-H bonds, C-X bonds (X for F, Cl and Br etc.) always appear more intense due to high accumulated local charge. [20] Secondly, we assign the lines η and γ to the hydrogen bonds of the C-H$\cdots$Cl type by considering its linear directionality. [21,22] If the bonds were assigned in the other way, then the following two scenarios will happen. 1. The hydrogen will be bending with a 90º angle which is in contrast to the linear directionality argument. 2. Position β will be where a Chloride atom locates thus the bond length of C11- β will be too long. However to make things clear, we suggest a controlled experiment with the Trichloroethylene molecule in the future. The adsorption site of the dimer is again obtained with a high-resolution topographic imaging using the CO tip with a set-point of 10 mV/0.5 nA and it is shown in Figure 4.8b. Except for the dashed lines of which the centered are marked by η and γ, all dashed lines in Figure 4.8a are indications where the apparent interactions between the dimer and the substrate which the itProbe image reveals in Figure 4.8c.

Figure 4.8: Constant-current itProbe imaging of the trans-$C_2H_2Cl_2$ dimer on Ag(110) surface. (A) Schematic diagram showing the adsorption of the dimer on Ag(110). Dash lines correspond to line features imaged by itProbe. The adsorption sites are extracted from the topographic image showing in (B). (B) Topographic image showing the adsorption site of the dimer on the Ag(110) surface and Ag atoms on the surface as resolved with a CO-tip at a set point of 10 mV/0.5 nA. White circles correspond to the positions over the Ag atoms. (C) Constant-current itProbe image of the trans-$C_2H_2Cl_2$ dimer taken at sample bias of 1.5 mV and tunneling gap set at 15 mV/0.1 nA. (D) Same itProbe image as in (C) with an overlay of the schematic diagram for the dimer, together with dashed lines between the two molecules and with the Ag(110) substrate. (E) *dI/dV* image at 1.5 mV recorded simultaneously with the itProbe image in (C). (F) Current image at 1.5 mV recorded simultaneously with the itProbe image. (G) Topographic image recorded when the tunneling set point is 15 mV/0.1 nA. (H) Topographic image recorded when the set point is 0.1 V/ 0.1 nA. Except for (B), which is 24 Å x 24 Å, all other images are of size 14 Å x 14 Å.
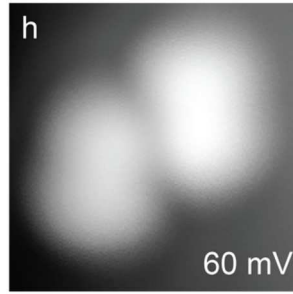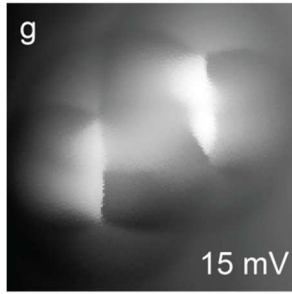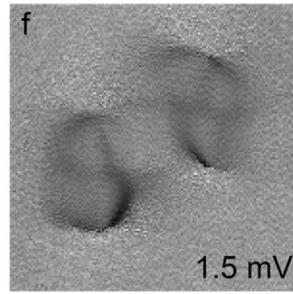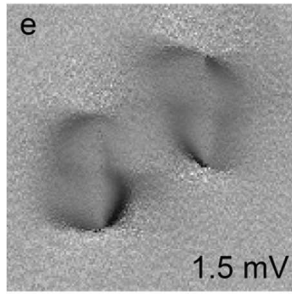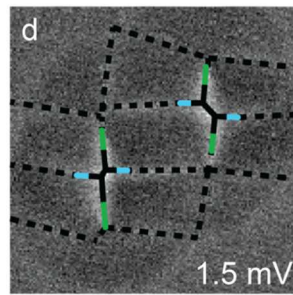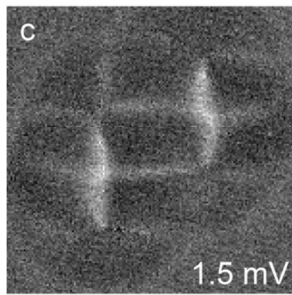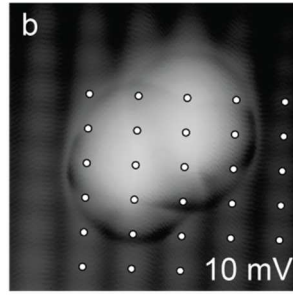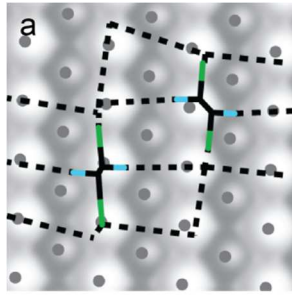
In summary, we investigated acyclic molecules using the state-of-the-art STM-itProbe imaging technique. Molecular bonding structures have been revealed for both a C_2H_4 molecule and a trans-1,2-dichloroethylene dimer. The C-C bond length and H-C-H bond angle resolved for C_2H_4 agree well with the theoretical values for a gas phase molecule. Particularly, the two degrees of freedom, i.e., the tunneling gap and probing sample bias, are comprehensively surveyed, suggesting a strong correlation between the itProbe images and the potential energy surface. The bonding structure of the trans-1,2-dichloroethylene molecule, shown in the dimer itProbe image, displays asymmetric shape and significantly differs from the symmetric structure revealed for the C_2H_4 molecule.

4.3 Bibliography

[1]   R. Temirov, S. Soubatch, O. Neucheva, A. Lassise, and F. Tautz, New Journal of Physics **10**, 053012 (2008).

[2]   L. Gross, F. Mohn, N. Moll, P. Liljeroth, and G. Meyer, Science **325**, 1110 (2009).

[3]   D. Oteyza, P. Gorman, Y.-C. Chen, S. Wickenburg, A. Riss, D. J. Mowbray, G. Etkin, Z. Pedramrazi, H.-Z. Tsai, A. Rubio, M. Crommie, and F. Fischer, Science **340**, 1434 (2013).

[4]   J. Zhang, P. Chen, B. Yuan, W. Ji, Z. Cheng, and X. Qiu, Science **342**, 611 (2013).

[5]   C. Chiang, C. Xu, Z. Han, and W. Ho, Science **344**, 885 (2014).

[6]   C. Weiss, C. Wagner, R. Temirov, and S. F. Tautz, Journal of the American Chemical Society **132**, 11864 (2010).

[7]   C Weiss, C Wagner, C Kleimann, M Rohlfing, and FS Tautz, Physical Review Letters **105**, 086103 (2010).

[8]   P. Hapala, G. Kichin, C. Wagner, S. F. Tautz, R. Temirov, and P. Jelínek, Physical Review B **90**, 085421 (2014).

[9]   P. Hapala, R. Temirov, F. Tautz, and P. Jelínek, Physical Review Letter **113**, 226101 (2014).

[10]   L. Gross, F. Mohn, N. Moll, B. Schuler, A. Criado, E. Guitián, D. Peña, A. Gourdon, and G. Meyer, Science **337**, 1326 (2012).

[11]   S. Kawai, A. Sadeghi, F. Xu, L. Peng, A. Orita, J. Otera, S. Goedecker, and E. Meyer, ACS Nano **9**, 2574 (2015).

[12]   JL Solomon, RJ Madix, and J Stöhr, The Journal of Chemical Physics **93**, 8379 (1990).

[13]   J. Hahn and W. Ho, Physical Review Letters **87**, 196102 (2001).

[14]   C Backx and C. Groot, Surface Science (1982).

[15]   C Backx, C. Groot, P Biloen, and W. Sachtler, Surface Science (1983).

[16]   N. Craig, P. Groner, and D. McKean, The Journal of Physical Chemistry A **110**, 7461 (2006).

[17]   U. Ham and W. Ho, The Journal of Chemical Physics **138**, 074703 (2013).

[18]   C. G. P. M. Bernardo and J. A. N. F. Gomes, Journal of Molecular Structure: THEOCHEM **582**, 159 (2002).

[19]   L. Vitali, R. Ohmann, K. Kern, A. Garcia-Lekue, T. Frederiksen, D. Sanchez-Portal, and A. Arnau, Nano Letters **10**, 657 (2010).

[20]   W. Ho et al., unpubished results.

[21]   M. Goswami and E. Arunan, Physical Chemistry Chemical Physics **11**, 8974 (2009).

[22]   T. Steiner, Angewandte Chemie International Edition **41**, 48 (2002).

Chapter 5 Conclusion and Prospect

With the aid of the state-of-the-art sub-Kelvin STM, we are able to push the energy resolution of single molecule vibrational spectroscopy to its limit, and made the observation of spin-flip IETS and spin-vibronic spectroscopy possible. The intrinsic IETS peak width decreases tremendously under 600 mK, and we are able to resolve more features that are not possible before. The line shape of single IETS peak is now easy to resolve. And we can correlate the asymmetry of the line shape to the geometry of the molecular tunnel junction. We even combine the spatial resolution of STM together with this energy resolution to invent a new imaging technique in resolving the bonding structure of molecule adsorbed on surfaces. However, the research with the sub-Kelvin STM is so far mainly focusing on single molecule vibration, the study on the spin degree of freedom still needs more exploration.

So far we are able to take itProbe image by recording the shift of vibrational IETS. We may also be able to record the shift of spin-flip IETS, if it is possible to attach an isolated spin to the tip. The isolation of the spin from the metal tip is a challenge and we have been looking for the right candidate for a long time. Attaching an isolated spin to the tip apex is different from the so-called

spin-polarized STM in that an external magnetic field is not a must for the latter technique, [1] while the spin-flip inelastic probe needs one in order to reveal the spin-flip IETS. If we are lucky to find such a candidate, then there is plenty of room to play. One possibility that one can think of is the generalization of chemical bonds to the so-called anti-ferromagnetic bonds, especially in a triangular lattice. In such a two-dimensional configuration, neighboring spins at the vertices of a triangle experience frustration and two out of those three couplings is different from the third one. [2] Therefore one may expect to see bonding structures resulting from the interactions between spins.

With single spin adsorbed on decoupling layers, there is a chance that we may observe Kondo effect instead. The Kondo effect is a phenomenon that isolated spin is screened by the spins of the conduction band from the underlying metal. With zero magnetic field, it manifests itself as a peak in the magnetic impurity's density of states at the Fermi level. Zeeman splitting can be observed once a magnetic field is applied. [3,4] By recording the variation of the Kondo splitting of the spin on the tip, we may depict the magnetic characteristics of the underlying molecule as well. Instead of peak at Fermi level, Kondo effect may be shown as Fano line shape in dI/dV spectrum, when the coupling of the magnetic impurity and the host metal is strong. [5,6] It is possible that magnetic property can also be probed with this Fano line shape spectrum. [7]

With any probing technique, either vibrational itProbe or spin-flip itProbe, there are two degrees of freedom that one can tune for constant height imaging. [8] One is the probing bias, which can be done easily. The other one is z, which so far we are done through feeding voltage to the inner piezo by a 12-bit DAC. It is considered as coarse and 1 bit output equals to about 0.3 Å, which may not be able to meet our needs. [9] With a 20-bit DAC, it is expect to achieve a tuning capability of about 0.1 picometer / bit. [10]

Bibliography

[1]   R. Wiesendanger, Reviews of Modern Physics **81**, 1495 (2009).

[2]   M. Collins and O. Petrenko, Canadian Journal of Physics **75**, 605 (1997).

[3]   A. J. Heinrich, J. A. Gupta, C. Lutz, and D. Eigler, Science 466 (2004).

[4]   U. Ham and W. Ho, The Journal of Chemical Physics **138**, 074703 (2013).

[5]   V. Madhavan, W. Chen, T. Jamneala, M. Crommie, and N. Wingreen, Science **280**, 567 (1998).

[6]   Y. Jiang, Y. Zhang, J. Cao, R. Wu, and W. Ho, Science **333**, 324 (2011).

[7]   M. Sato, H. Aikawa, K. Kobayashi, S. Katsumoto, and Y. Iye, Physical Review Letters **95**, 066801 (2005).

[8]   C. Chiang, C. Xu, Z. Han, and W. Ho, Science **344**, 885 (2014).

[9]   J. Bork, Y. Zhang, L. Diekhöner, L. Borda, P. Simon, J. Kroha, P. Wahl, and K. Kern, Nature Physics **7**, 901 (2011).

[10]   U. Ham, Ph.D. thesis, University of California, Irvine

Appendix: Manuals

A.1   Tip Sputtering and Annealing Bipolar Controller

Once tips are loaded into vacuum chamber, each tip needs further processing for cleaning and sharpening before introduction to the scanner. The top two drawings in Figure A 1.1 show the schematics for tip annealing and sputtering, respectively.

During tip annealing, high current is applied the filament in order to generate free electrons, these electrons will then be accelerated towards the tip by the 1 kV applied between the heater and the tip, thus annealing the tip and removing any contamination introduced during the making of the tip, here the filament is electrically connected with the heater, so the filament and the heater are at equal potential. The current that is applied on the filament is typically 5 A.

While during self-sputtering, the polarity of the high voltage is reversed and Ne is introduced into the chamber for ionization. The self-ionized Ne^+ will be accelerated and bombard the tip, thus removing any residue on the tip. Typically the sharper the tip is, the larger the ion-current will be. For silver tip, the record is 2 μA which can be seen in STM-VI.

The procedure in mk-STM is degassing with tip inside the heater for 5 min and filament current at 5 A. Then it follows three cycles of sputtering and annealing.

Figure A 1.1: Schematic diagram for tip and sample sputtering and annealing

Annealing

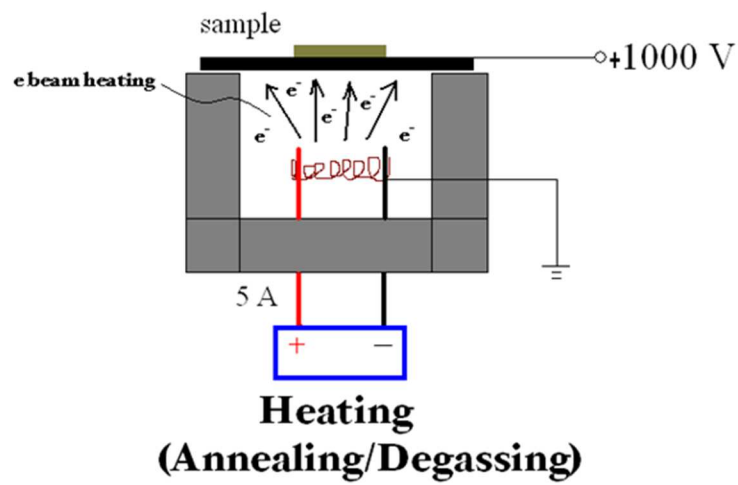**Self Sputtering**
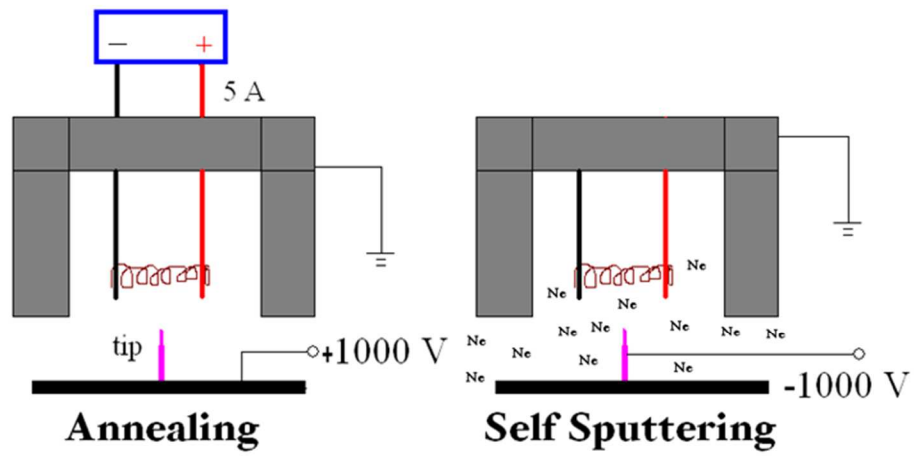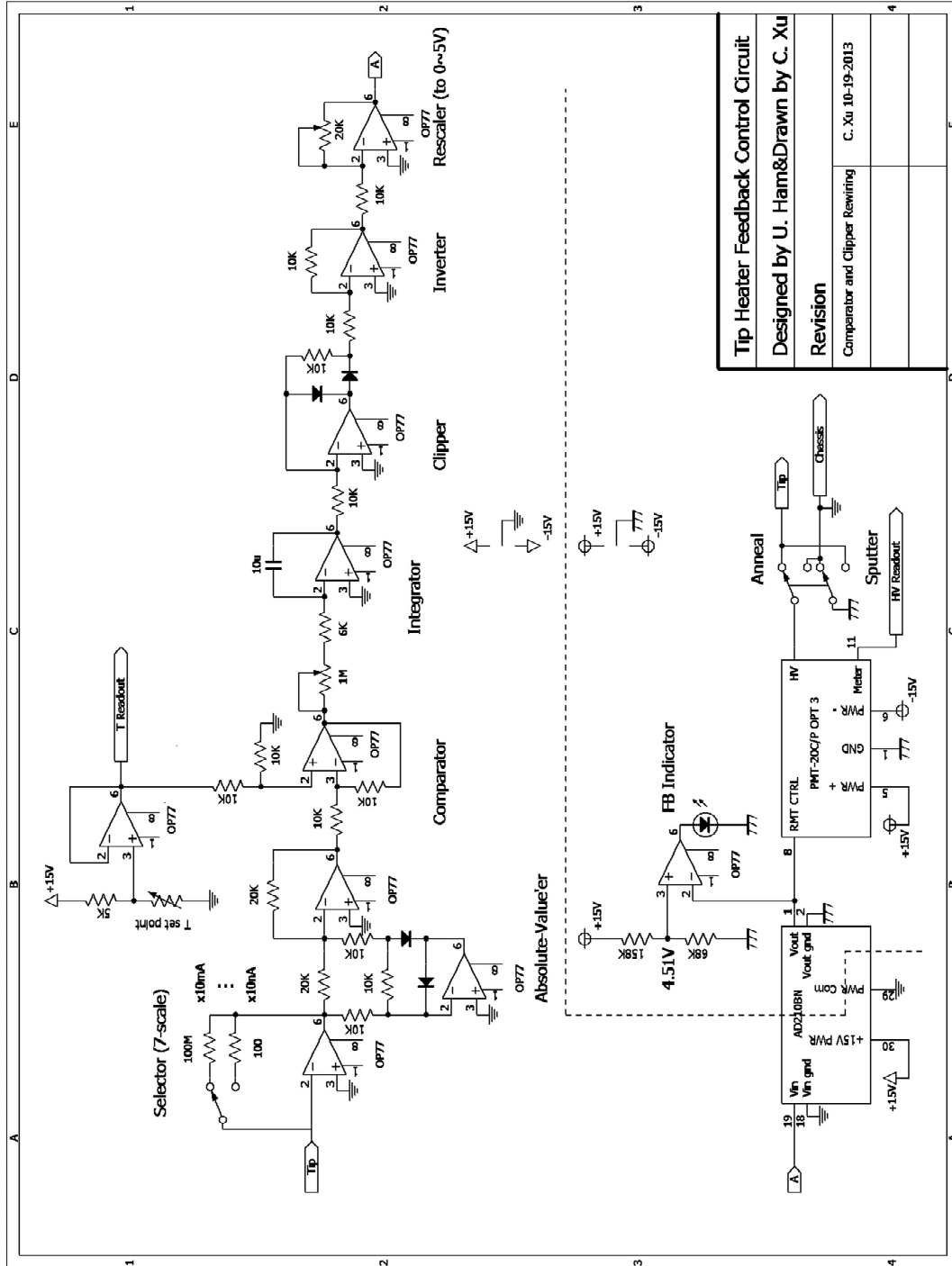
**Heating
(Annealing/Degassing)**

Figure A 1.2: Wiring diagram for the main circuit of the controller. Credit should be directed to Ungdon Ham who initiated and designed the diagram. Some modifications and improvements were made by me during the building and testing of the controller.
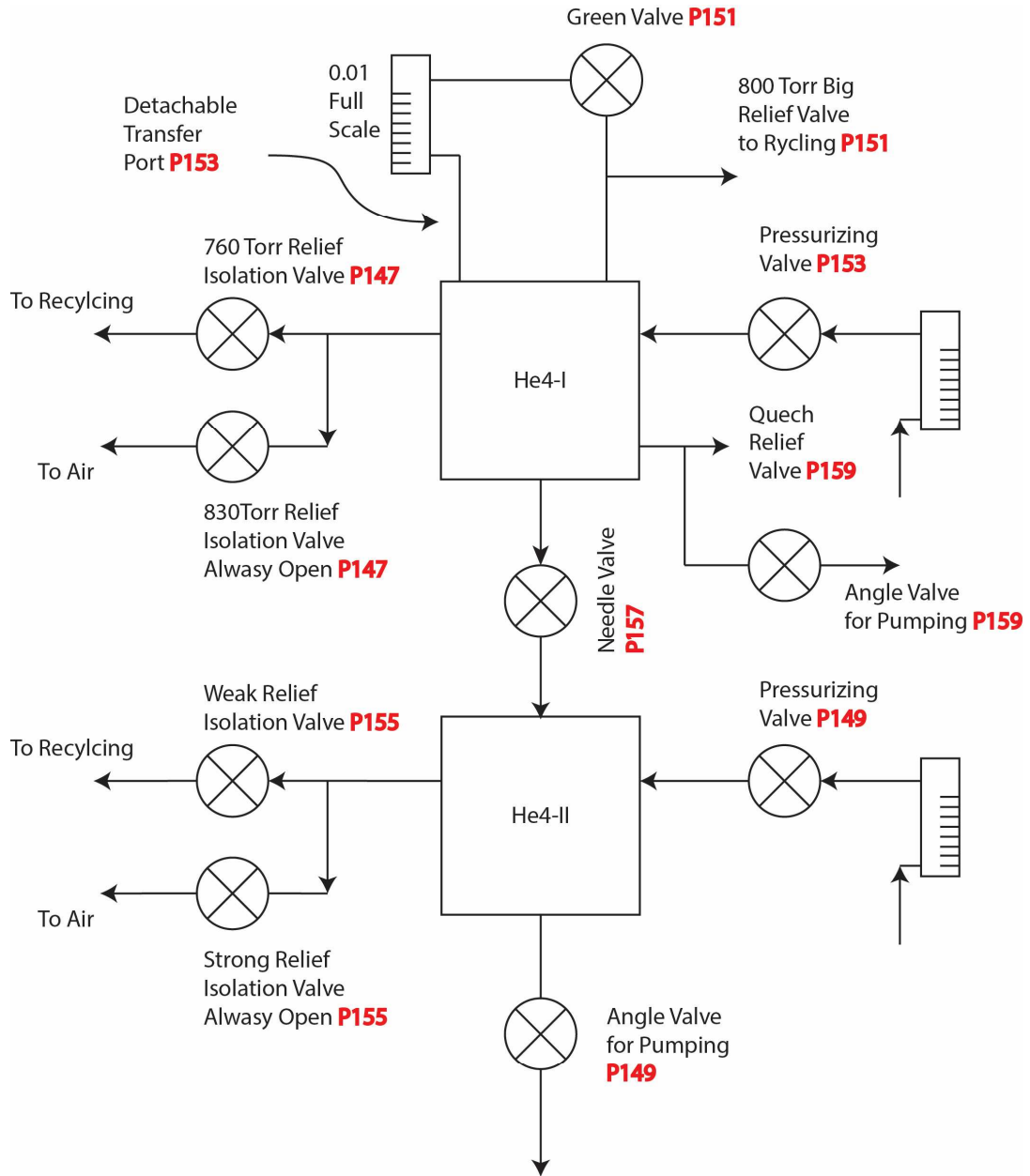
Rescaler (to 0~5V)

20K
OP77
10K

Inverter
10K
OP77
10K

Clipper
10K
OP77
10K

Integrator
10u
OP77
6K

+15V
-15V
+15V
-15V

Comparator
1M
10K
OP77
10K
T Readout
10K

Selector (7-scale)
x10mA
x10nA
100M
100
OP77
Tip
20K
10K
20K
10K
OP77
T set point
5K
+15V

Absolute-Value'er
10K
10K
OP77
OP77

FB Indicator
OP77
+15V

AD210BN
Vin
Vin gnd
19
18
+15V PWR
30
+15V
PWR
Com
29
Vout
Vout gnd
1
2
158K
4.51V
68K

RMT CTRL
HV
PMT-20C/P OPT 3
PWR
GND
PWR
Meter
8
5
6
11
+15V
-15V

Anneal
Tip
Chassis
Sputter
HV Readout

Tip Heater Feedback Control Circuit

Designed by U. Ham&Drawn by C. Xu

Revision
Comparator and Clipper Rewiring
C. Xu 10-19-2013
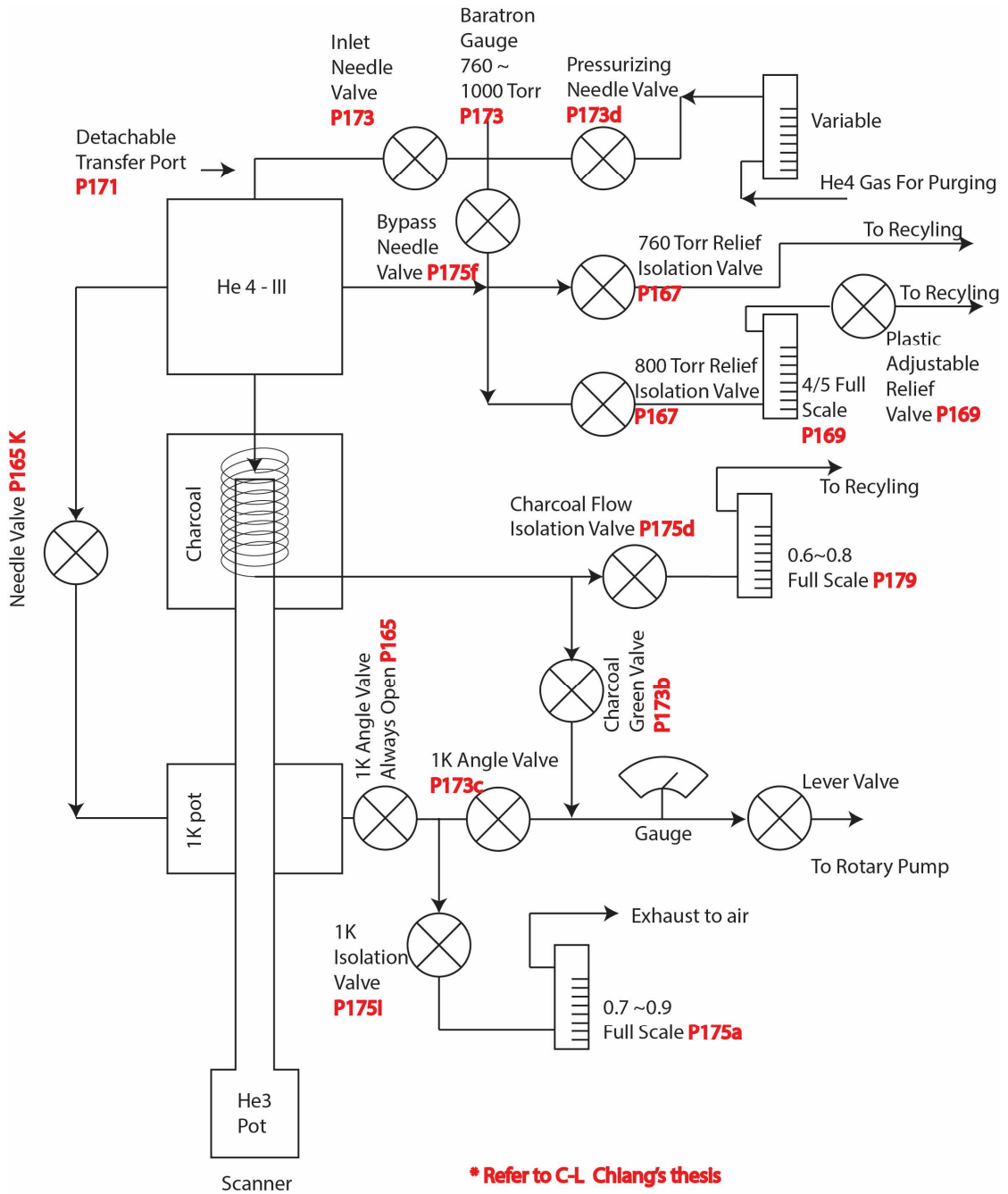
A.2 MK He4 Path Schematics

Schematic diagrams are attached for better understanding and maintenance of the He4-I II and III Dewars for mk-STM.

.

Figure A 2.1: Schematic diagram for He4-I and He4-II for mk-STM

Green Valve **P151**

0.01
Full
Scale

Detachable
Transfer
Port **P153**

800 Torr Big
Relief Valve
to Rycling **P151**

760 Torr Relief
Isolation Valve **P147**

Pressurizing
Valve **P153**

To Recylcing

He4-I

To Air

Quech
Relief
Valve **P159**

830Torr Relief
Isolation Valve
Alwasy Open **P147**

Angle Valve
for Pumping **P159**

Needle Valve
P157

Weak Relief
Isolation Valve **P155**

Pressurizing
Valve **P149**

To Recylcing

He4-II

To Air

Strong Relief
Isolation Valve
Alwasy Open **P155**

Angle Valve
for Pumping
P149

* Refer to C-L Chiang's thesis

89

Figure A 2.2: Schematic diagram for He4-III for mk-STM

A.3 Lateral Translational Stepping Function for the Traditional Scanner of the Besocke Type

In order to step the sample laterally, the core idea is to direct the coarse motion to the x, y directions. Before modification, the coarse mode is activated only when we rotate the sample, i.e. only during the processes of step up, step down or tip approach motion. The new modification forces the coarse mode to be on while keeping the translational motion activated. Notice that when directing the motion of step up/down to the x-y in-plane motion, only the motions along the ±x-direction can be realized without modifying the DSP code. In order to move the sample along the ±y-direction, GIANT_2 and ONEGIANT_2 need to be added to the DSP code. The code snippet that I modified is attached below and the keys for this modification are highlighted.

Figure A 3.1 shows the top view of the scanner, and this is the reference when using this new function. Figure A 3.2 shows the GUI for this module. When translational motion is activated, all the other buttons for starting rotational motions will be disabled. The translational motion shares the same parameters though, such as 'Approach Parameters' and 'Steps' etc. with slight deferent meanings.

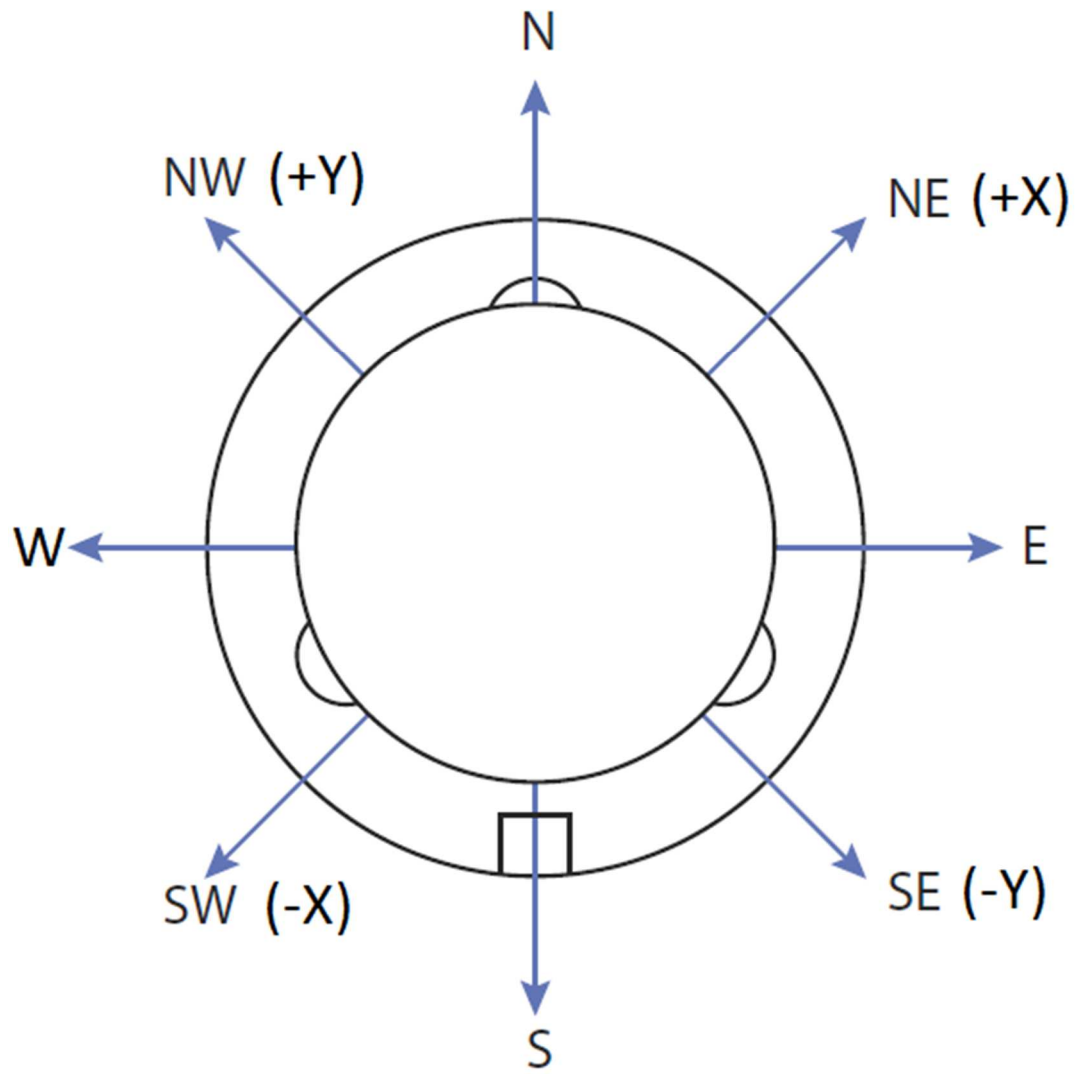Figure A 3.1: Schematic illustration of a Besocke type scanner

Figure A 3.2: Front panel of the modified version of Tip Approach GUI

The modified DSP codes can translate the sample in all 4 directions with no problem. However, when we start to poke tip using the deposition module, the program will freeze, further modification is necessary for full compatibility. So far I have no idea why this two isolated modules interfere with each other in any way. Therefore, as of 08/2015, the DSP for mk-STM is still in the un-modified version, meaning only the $\pm$x-direction motion can be activated, starting a motion in $\pm$y-direction will freeze the program and the DSP needs to be reset. The program with the translation module is available in the folder 'STM20Rev6.5'. (A modified DSP board is stored in the cabinet of MK for future reference)

```
;**************************************************************
; EQUIVALENTS
;**************************************************************
CMDVERSION   EQU $76      ;'v'
CMDOUTPUT    EQU $6F      ;'o'
CMDINPUT     EQU $69      ;'i'
CMDDELAY     EQU $64      ;'d'
CMDSQUARE    EQU $71      ;'q'
CMDRAMP      EQU $72      ;'r'
CMDRAMPREAD  EQU $52      ;'R'
CMDTIPSETUP  EQU $74      ;'t'
CMDGIANT     EQU $67      ;'g'
CMDGIANT_2   EQU $61      ;'a' alternative translation movement
direction
CMDAPPROACH  EQU $54      ;'T'
CMDMINUS     EQU $2D      ;'-'
CMDPLUS      EQU $2B      ;'+'
CMDSTOP      EQU $21      ;'!'
CMDSCANSETUP EQU $73      ;'s'
CMDSCANLINE  EQU $53      ;'S'
CMDHIGHRES   EQU $48      ;'H'
CMDHIGHERRES    EQU $58      ;'X'
CMDTRACKSETUP EQU $6B    ;'k'
CMDTRACK     EQU $4B      ;'K'
TRACKCONT    EQU $63      ;'c' to continue tracking
CMDRSSETUP   EQU $51      ;'Q'
CMDSPSETUP   EQU $79      ;'y'
CMDSPEC      EQU $59      ;'Y'
CMDDIAGSETUP EQU $6C      ;'l'
CMDDIAG      EQU $4C      ;'L'
CMDHOPSETUP  EQU $6A      ;'j'
CMDHOP       EQU $4A      ;'J'
CMDDEPSETUP  EQU $70      ;'p'
CMDDEP       EQU $50      ;'P'
CMDUPDATE    EQU $23      ;'#'


;**************************************************************
; MAIN_LOOP
; Receive and handle stm control characters via serial.
;**************************************************************
MAIN_LOOP

    jclr    #2,x:M_SSR,*    ;bit set when receive buffer full
                            ;until then, jmp to self
    movep   x:M_SRXL,a      ;receive serial data


    move    #>CMDSCANLINE,x0
    cmpu    x0,a
    beq     SCANLINE
    move    #>CMDSCANSETUP,x0
    cmpu    x0,a
    beq     SCANSETUP
```

```
move      #>CMDRSSETUP,x0
cmpu      x0,a
beq       READSEQSETUP
move      #>CMDSPSETUP,x0
cmpu      x0,a
beq       SPECSETUP
move      #>CMDSPEC,x0
cmpu      x0,a
beq       SPEC
move      #>CMDMINUS,x0
cmpu      x0,a
bclr      #0,r1
beq       AUTO
move      #>CMDPLUS,x0
cmpu      x0,a
bset      #0,r1
beq       AUTO
move      #>CMDDEPSETUP,x0
cmpu      x0,a
beq       DEPSETUP
move      #>CMDDEP,x0
cmpu      x0,a
beq       DEPOSITION
move      #>CMDTRACKSETUP,x0
cmpu      x0,a
beq       TRACKSETUP
move      #>CMDTRACK,x0
cmpu      x0,a
beq       TRACK
move      #>CMDAPPROACH,x0
cmpu      x0,a
beq       TIPAPPROACH
move      #>CMDGIANT,x0
cmpu      x0,a
beq       GIANT
move      #>CMDGIANT_2,x0
cmpu      x0,a
beq       GIANT_2
```

```
;*************************************************************
; GIANT_2, ONEGIANT_2, to move in NW and SE directions
; Performs giant steps.
;   TOUCHES: a, b, x0, x1, y0, y1 (mostly via subroutines)
;   USES: (r0) : max number of giant steps
;         (r1) : flags
;         (r3) : channel, passed to PARABOLA
;         (r4) : start for PARABOLA
;         (r6) : multiplier for PARABOLA
;         (r7) : end for PARABOLA
;   FLAGS: see TIPAPPROACH flags
;*************************************************************
GIANT_2

    jsr     RECEIVETWO  ; receive number of steps + direction (2
bytes)
    move    a1,r0

    bset    #2,r1
    bclr    #15,r0      ; test and clear direction bit
    bcs     GIANTUP_2
    bclr    #2,r1
GIANTUP_2

    do      r0,ONESTEP_2

    jsr     ONEGIANT_2

    ; check for serial input and enddo if necessary
    jset    #2,x:M_SSR,STOPSTEPS_2
    jmp     PROCEED_2
STOPSTEPS_2
    clr     a
    movep   x:M_SRXL,a1
    move    #>CMDSTOP,x0
    cmpu    x0,a
    nop
    brkeq

PROCEED_2
    ; send control character via serial for each step completed
    DELAY   #>100               ;unnecessary?
    move    #>CMDGIANT_2,a
    jclr    #0,x:M_SSR,*        ;bit set when transmit buffer empty
                                ;until then, jmp to self
    movep   a1,x:M_STXL         ;send byte

ONESTEP_2
    jmp     MAIN_LOOP


;*************************************************************
; ONEGIANT_2 (see above)
;*************************************************************
```

100

```
ONEGIANT_2

    bset    #0,r1
    btst    #2,r1
    bcs     PARABUP_2
    bclr    #0,r1
PARABUP_2

    ; pre-parabola: just output zero volts to x
    move    #>ZERO,a
    move    #>YCH,y1
    jsr     OUTPUTBITS
    move    y:Tip_X_Zero,y0
    do      y0,DUNXZERO_2
    DELAY   #>DIOOUTTIME
DUNXZERO_2

    ; output x parabola
    move    #>YCH,r3
    move    #>ZERO,r4
    move    y:Tip_X_Mult,r6
    move    y:Tip_X_Step,y0
    move    #>ZERO,a
    jclr    #0,r1,DOWNTARGET_2
    add     y0,a
    jmp     DUNTARGET_2
DOWNTARGET_2
    sub     y0,a
DUNTARGET_2
    move    a1,r7
    bclr    #1,r1                       ; normal parabola, *not* inverted

    jsr     PARABOLA

    ; set zouter to step value
    move    y:Tip_Zo_Step,y0
    move    y0,a
    move    #>ZERO,y0
    add     y0,a
    move    a1,r4
    move    #>ZOCH,y1
    jsr     OUTPUTBITS

    ; delay 5 * output time
    do      #>5,RELAXATION_2
    DELAY   #>DIOOUTTIME
RELAXATION_2

    ; relax x
    move    #>ZERO,a
    move    #>YCH,y1
    jsr     OUTPUTBITS
```

101

```
                ; do tip delay
                move    y:Tip_Delay,y0
                DELAY   y0

                ; output zouter parabola - 1st half
                move    #>ZOCH,r3
                move    y:Tip_Zo_Mult,r6

                ; calculate target
                move    y:Tip_Zo_Step,y0
                move    y0,a
                lsr     a                   ; Step/2 is size of half-parabola
                move    #>ZERO,y1
                add     y1,a
                move    a1,r7

                bclr    #0,r1               ; decreasing parabola
                bclr    #1,r1               ; normal parabola, *not* inverted
                jsr     PARABOLA

                ; output zouter parabola - 2nd half (inverted)
                move    r7,r4
                move    #>ZERO,r7
                bset    #1,r1               ; inverted parabola
                move    x1,a
                move    #>1,x1
                sub     x1,a
                move    a1,x1
                jsr     PARABOLA

                ;output zero to zouter
                move    #>ZERO,a
                move    #>ZOCH,y1
                jsr     OUTPUTBITS

                rts
```

A.4 LabVIEW Program for Controlling Liquid Helium Recycling

In principle the higher the working pressure is, the higher the helium liquefaction rate will be, of course, the pressure should be below the critical point. Here we use PID feedback algorithm to control the incoming Helium gas flow in order to maintain a high and stable working pressure inside the liquefier dewar. As of 05/2015 we have a steady yield of about 25 LHe per cold head per day when maintaining the working pressure at 14.5 Psig.

For LabVIEW programming, Greg wrote the code for the Temperature Monitoring module and I wrote the rest of the code. I finally decided to go with sub-panel scheme in order to combine different modules into a single software. Figure A 4.1 shows a typical functioning PID feedback fine tuning the mass flow set-point. In Figure A 4.2, the part circled in A 4.2.1 is the ones utilizing the sub-panel function. Notice that once they are embedded inside separate subpanels, they are isolated programs and are no longer able to communicate with each other.

In order to have the Mass Flow Controller talk to the Liquefier pressure sensors, these two modules needs to be in the same subpanel so that a PID algorithm can be implemented.

The code circled inside A 4.2.2 in figure A 4.2 is for the purpose of logging all the parameters. A Master-Slave framework was employed in case of memory leak.

Further improvements include finer tuning of the PID parameters and error handling of each VISA read/write block.

All the VISA interface documentation can be found in the folder 'Liquefier Files' inside the Ho-Group Dropbox.

Figure A 4.1: LabVIEW front panel for the liquid recycling system

106

Figure A 4.2: LabVIEW block panel for the liquid recycling system main logger
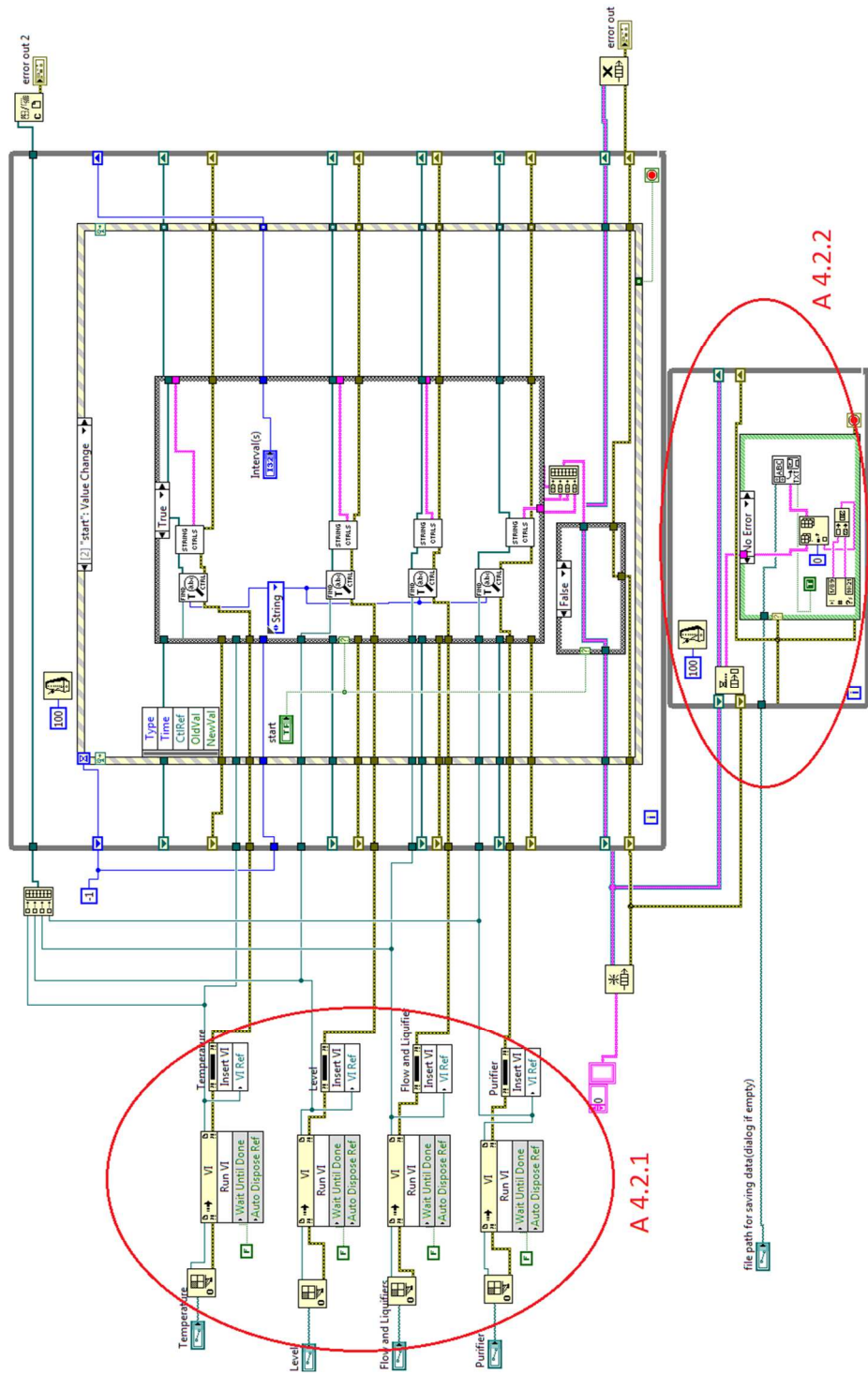
A.5 Helium Gas Buffer Bag Interface with the Bauer Compressor

The Bauer Compressor comes with interface which allows customized signal triggering. A schematic diagram employed sensors sensing the height of the buffer helium gas bag was designed for controlling the activation/deactivation of the compressor. (Note that the Pressure Switch Settings have higher priority in control than this activator.) A warning sign is posted on the front panel of the compressor in case of accidental deactivation of this activator, since a manual deactivation through the front MAPLE panel will bypass it unless the activator is restarted.

A USB relay was employed to remotely 'Force to Turn ON' the compressor. The Python code is attached below for reference.

After a discussion with Calvin, we figured out the compressor is using edge triggering rather than level triggering, and that's the reason why any front panel operation will bypass the activator. And that makes things complicate. Rather than spending time fiddling with chips, I think using an Arduino® development kit might be more efficient and even cheaper for any future upgrade.

(Update) As of Jan. 2016, a new control box with Arduino® by one of the visiting students is finished. Refer to the manual in the main server for further information.

Figure A 5.1: Wring diagram version 1.0 for the helium gas buffer bag interface with the Bauer compressor

Bauer Compressor Control Box
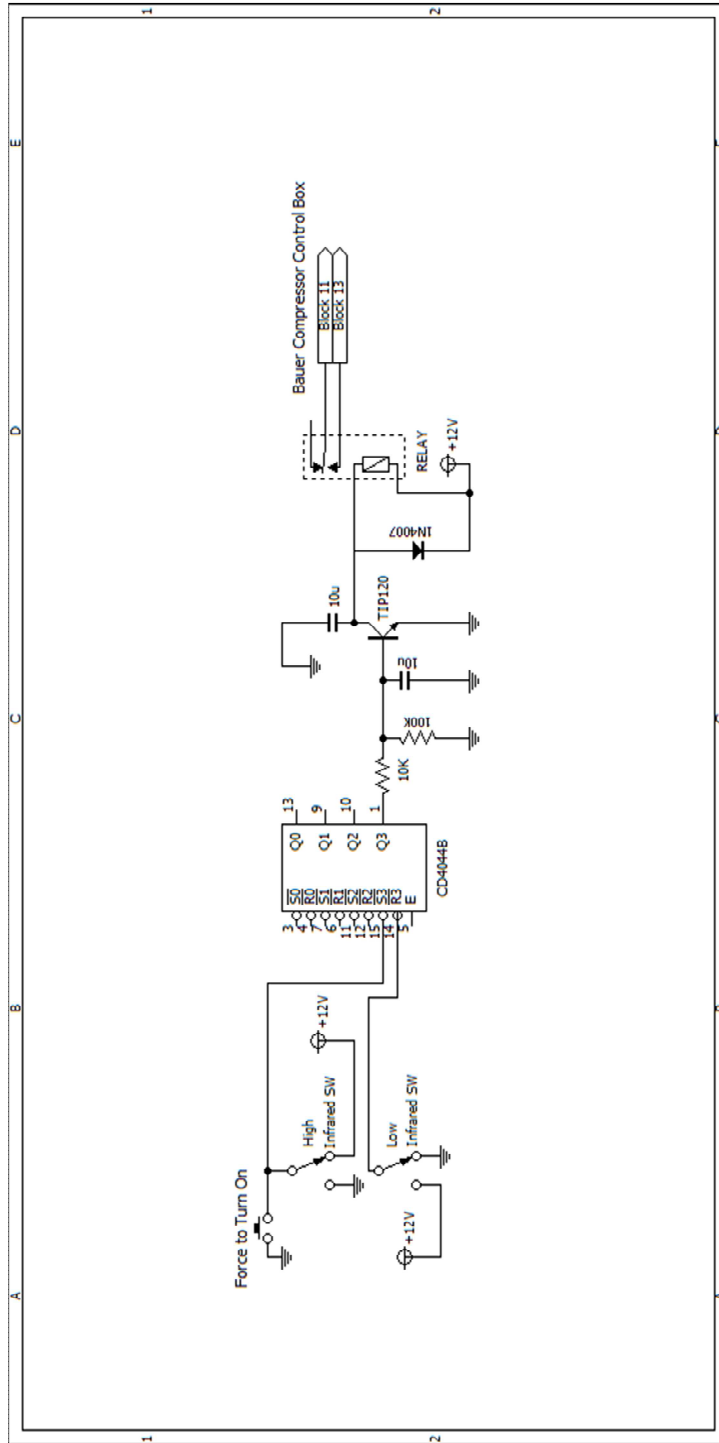
```python
from Tkinter import *
import serial
import time
import Queue
import threading


class Example(Frame):

  def __init__(self, parent):

    Frame.__init__(self, parent, background="white")
    self.queue = Queue.Queue()
    self.parent = parent

    self.statusLabel = StringVar(parent)
    self.statusLabel.set('Idle')
    self.comport = StringVar(parent)
    self.initUI()


  def initUI(self):

    self.parent.title("Compressor")
    self.pack(fill=BOTH, expand=1)

    self.label = Label(self, textvariable = self.statusLabel)
    self.label.pack()

    choices = ['COM'+ str(i) for i in range(20)]
    self.comport.set('COM1')
    self.option = OptionMenu(self, self.comport, *choices)
    self.option.pack()

    self.button = Button(self, text = 'Compress', command =
self.press)
    self.button.pack()

  def press(self):
    self.button.config(state = "disabled")
    self.thread = ThreadedClient(self.queue, self.comport.get())
    self.thread.start()
    self.periodiccall()
  def periodiccall(self):
    self.checkqueue()
    if self.thread.is_alive():
      self.after(100, self.periodiccall)
    else:
      self.button.config(state="active")
  def checkqueue(self):
    while self.queue.qsize():
      try:
        msg = self.queue.get(0)
        self.statusLabel.set(msg)
```

```python
        except Queue.Empty:
            pass

class ThreadedClient(threading.Thread):
    def __init__(self, queue, comport):
        threading.Thread.__init__(self)
        self.comport = comport
        self.queue = queue
    def run(self):

        try:
            serPort = serial.Serial(self.comport, 19200, timeout=1)
        except serial.SerialException:
            self.queue.put('Serial Error')
        else:
            serPort.write("relay "+ 'on' +" "+ '0' + "\n\r")
            time.sleep(1)
            serPort.write("relay read "+ '0' + "\n\r")
            time.sleep(1)
            response = serPort.read(50)
##          print 'on--' + response
            if(response.find("on\n") > 0):
                msg = 'Relay ON'
            elif(response.find("off\n") > 0):
                msg = 'Relay OFF'
            else:
                msg = 'Relay status unknown'
            self.queue.put(msg)
            time.sleep(1)
            serPort.write("relay "+ 'off' +" "+ '0' + "\n\r")
            time.sleep(1)
            serPort.write("relay read "+ '0' + "\n\r")
            time.sleep(1)
            response = serPort.read(50)
##          print 'off--' + response
            if(response.find("on\n") > 0):
                msg = 'Relay ON'
            elif(response.find("off\n") > 0):
                msg = 'Relay OFF'
            else:
                msg = 'Relay status unknown'
            self.queue.put(msg)

def main():

    root = Tk()
    root.geometry("250x100+300+300")
    app = Example(root)
    app.mainloop()

if __name__ == '__main__':
    main()
```

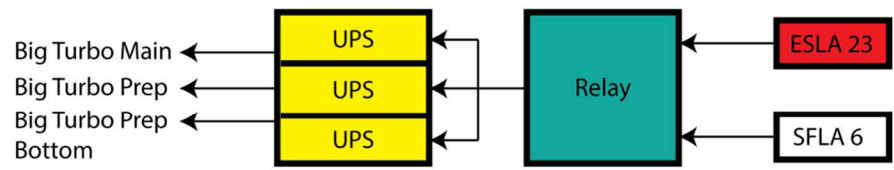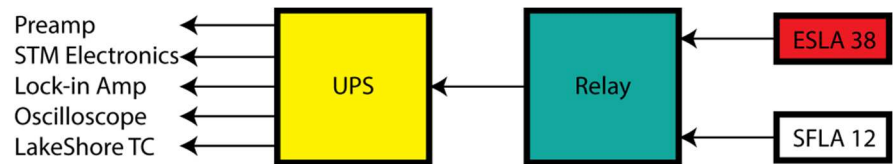## A.6 MK Power Connection Schematics

The mk-STM power connection schematics are attached to facilitate maintenance and future electronics installation. The power outlets with label 'ESLA' are emergency power colored in red, and the ones with label 'SLZL/M' are standard unfiltered power colored in black. The rest with label 'SFLA' are standard filtered power colored in white.

Figure A 6.1: Legend for the electrical diagrams for mk-STM system

ESLA	Emergency Power
SLZL	Normal Power
SFLA	Normal Power for Sensitive Electronics
	Power Strip
	Uninterruptible Power Supply (UPS)
	Relay
	Anti-Automatic Restart Protection (AARP)

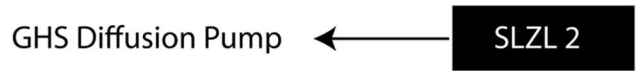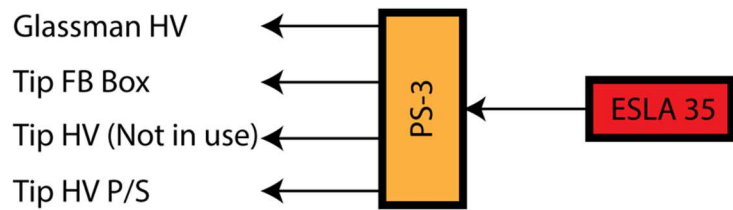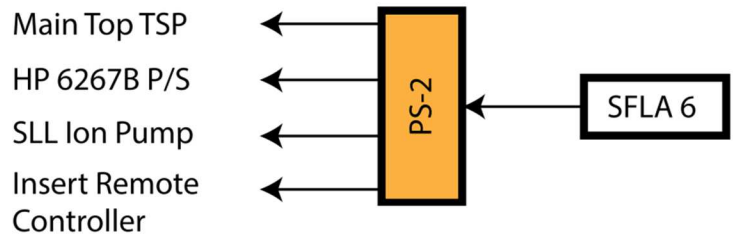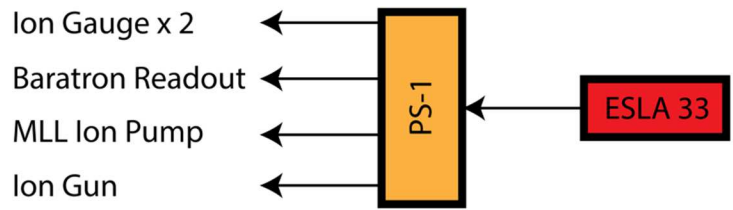|	
AARP:	Anti-Automatic Restart Protection
Amp:	Amplifier
COM:	Power Strip for computers
DMM:	Digital Multi-Meter
EV:	Evaporator
FB:	Feedback
GHS:	Gas Handling System
HV:	High Voltage
MLL:	Molecular Load Lock
Prep:	Preparation Chamber
PS:	Power Strip
P/S:	Power Supply
TC:	Thermalcouple
TSP:	Titanium Sublimation Pump
SLL:	Sample/tip Load Lock
SV:	Solenoid Valve
UPS:	Uninterruptible Power Supply

Figure A 6.2: mk-STM electrical schematic diagram part-1

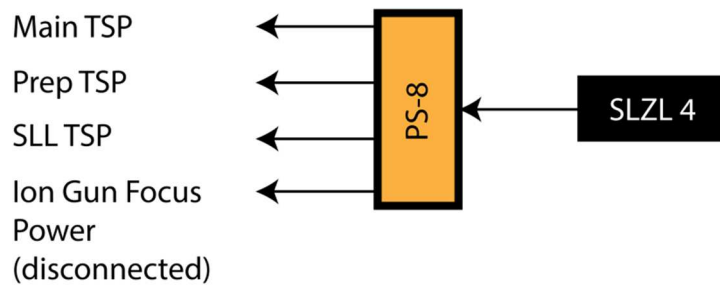Preamp ← UPS ← Relay ← ESLA 38
STM Electronics ←
Lock-in Amp ←
Oscilloscope ←
LakeShore TC ←   Relay ← SFLA 12

Big Turbo Main ← UPS ← Relay ← ESLA 23
Big Turbo Prep ← UPS ← Relay
Big Turbo Prep Bottom ← UPS ← SFLA 6

220V Main Top Ion Pump* ← Relay ← ESLA 25/27
220V Main Ion Pump ← Relay
220V SLL Ion Pump (disconnected) ← SFLA 8/10

110V Prep Ion Pump* ← UPS ← ESLA 37
Pyrometer ← UPS
Sample Heater FB Box ← UPS
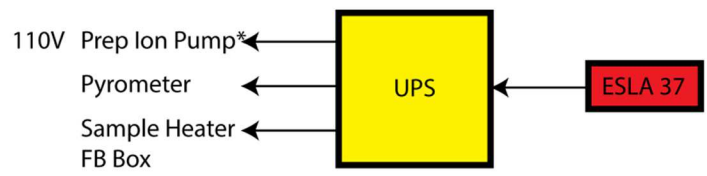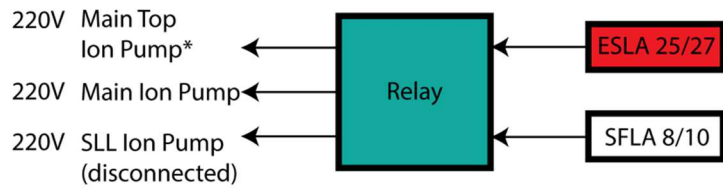
*These two controllers were swapped
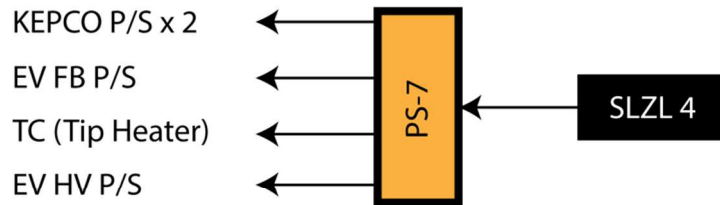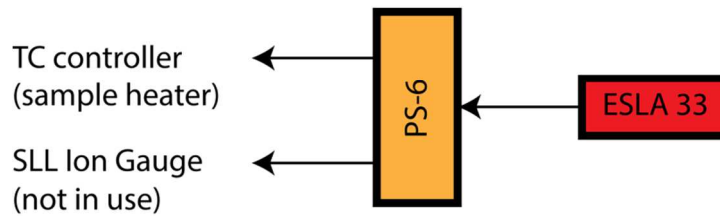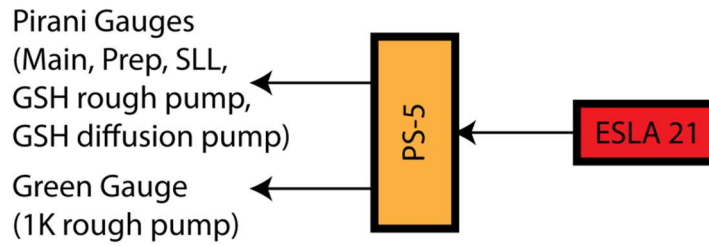
118

Figure A 6.3: mk-STM electrical schematic diagram part-2
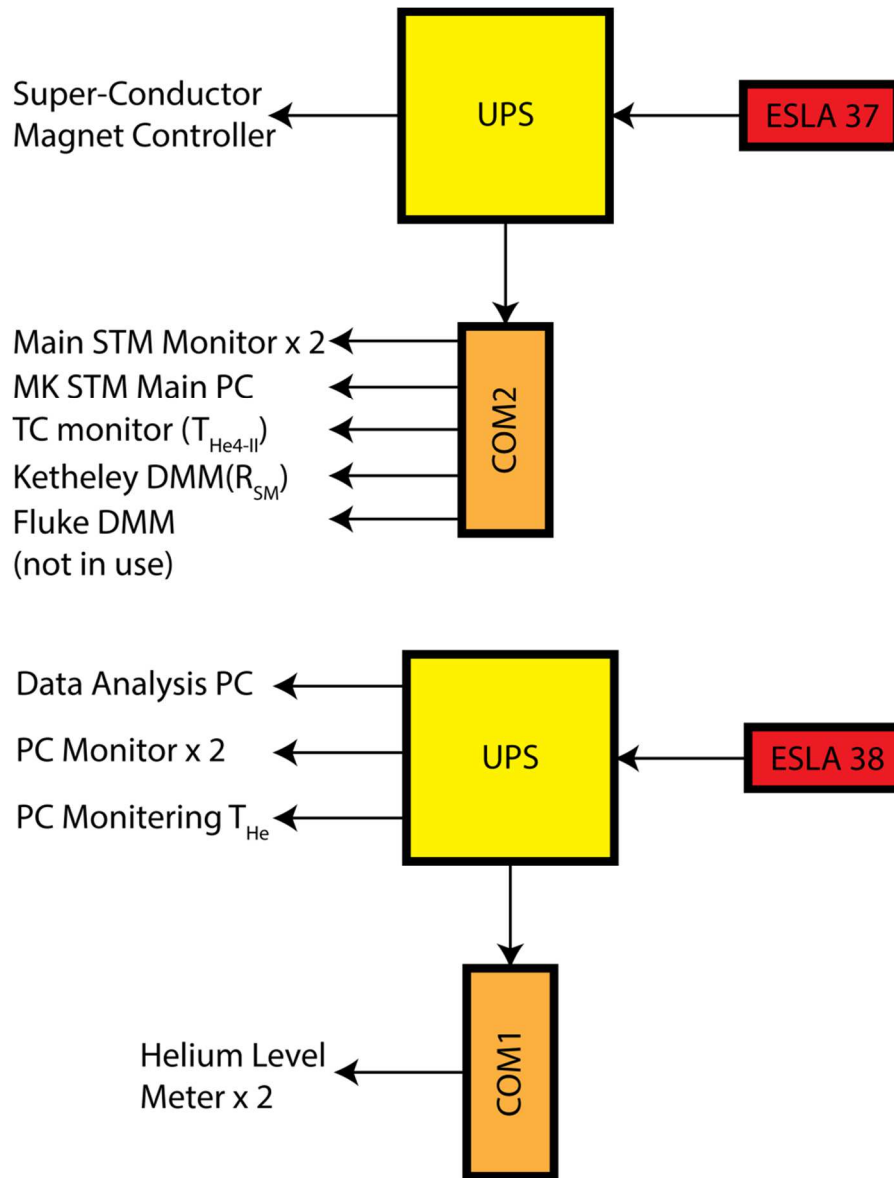
Figure A 6.4: mk-STM electrical schematic diagram part-3
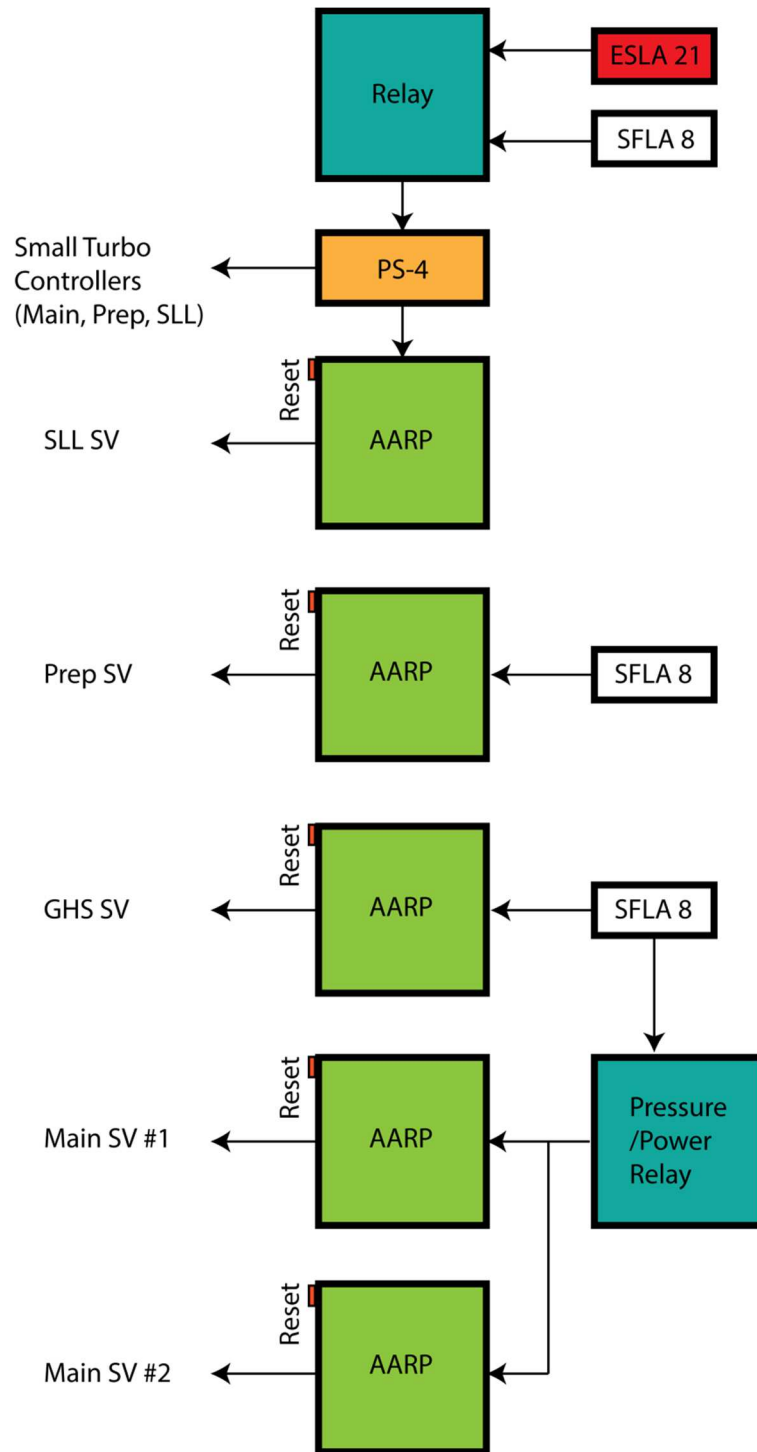
Figure A 6.5: mk-STM electrical schematic diagram part-4

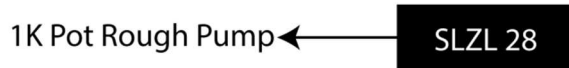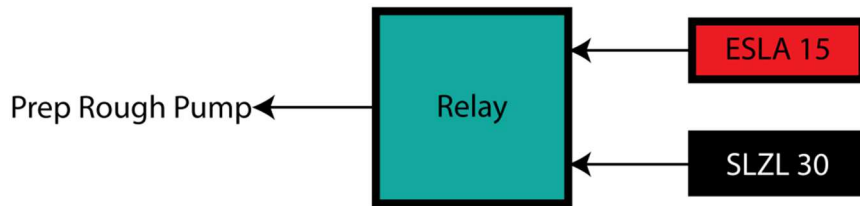Ion Gauge x 2 ← PS-1 ← ESLA 33

Baratron Readout ← PS-1

MLL Ion Pump ← PS-1

Ion Gun ← PS-1

Main Top TSP ← PS-2 ← SFLA 6

HP 6267B P/S ← PS-2

SLL Ion Pump ← PS-2

Insert Remote Controller ← PS-2

Glassman HV ← PS-3 ← ESLA 35

Tip FB Box ← PS-3

Tip HV (Not in use) ← PS-3

Tip HV P/S ← PS-3

GHS Diffusion Pump ← SLZL 2

HP6260B P/S ← ESLA 39/41

Cold Cathode Controller monitering Main, Prep and SLL Small turbos' inlets ← SFLA 8
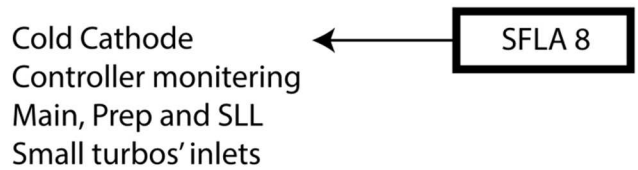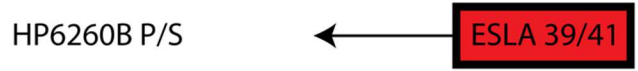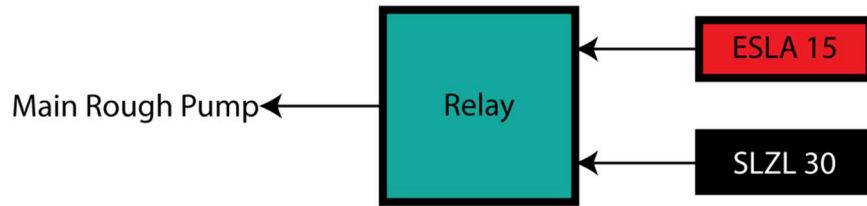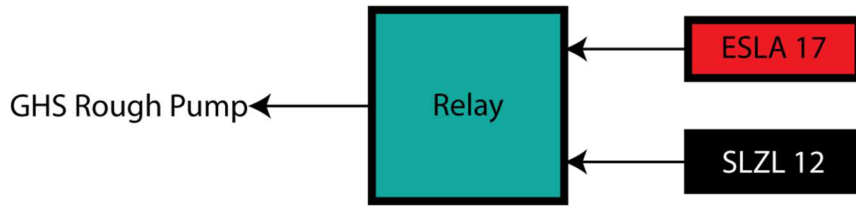
Figure A 6.6: mk-STM electrical schematic diagram part-5

Pirani Gauges
(Main, Prep, SLL,
GSH rough pump,
GSH diffusion pump) ← PS-5 ← ESLA 21

Green Gauge
(1K rough pump) ←

TC controller
(sample heater) ← PS-6 ← ESLA 33

SLL Ion Gauge
(not in use) ←

KEPCO P/S x 2 ←

EV FB P/S ← PS-7 ← SLZL 4

TC (Tip Heater) ←

EV HV P/S ←

Main TSP ←

Prep TSP ← PS-8 ← SLZL 4

SLL TSP ←

Ion Gun Focus
Power
(disconnected) ←

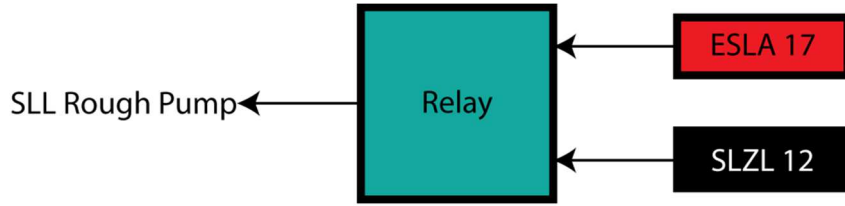Figure A 6.7: mk-STM electrical schematic diagram part-6

Figure A 6.8: Photo of mk-STM electrical instruments rack #1

TC controller
(sample heater)

Pyrometer

Ion gauge x 2

Baratron
Readout

Ion Gun
Controller

Big Turbo
Controller x 3

120V Prep Ion
Pump Controller

220V Main Top
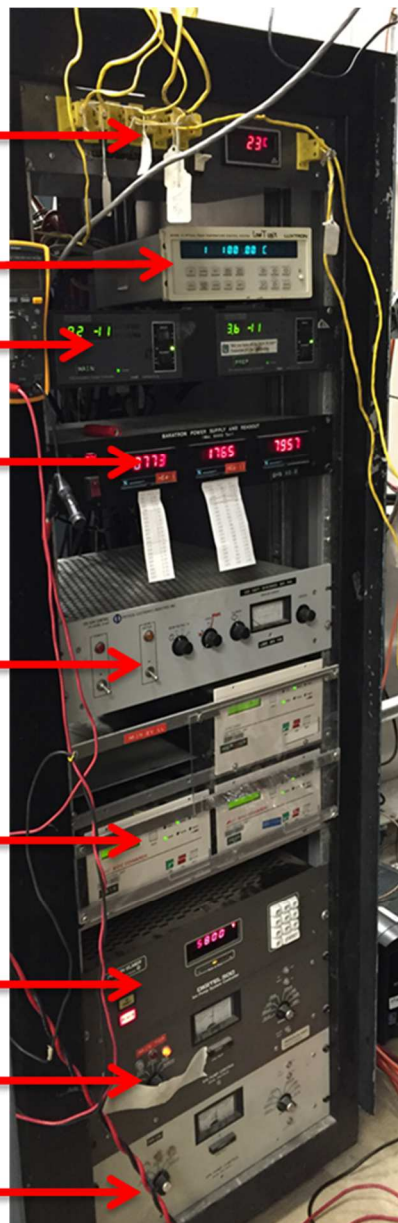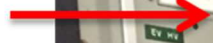Ion Pump Controller
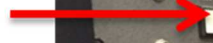
220V Main Ion
Pump Controller

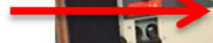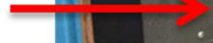Figure A 6.9: Photo of mk-STM electrical instruments rack #2

EV HV

EV FB

KEPCO
P/S x 2

HP 6260B

Sample
Heater
FB Box

Prep TSP

Main TSP

LL TSP
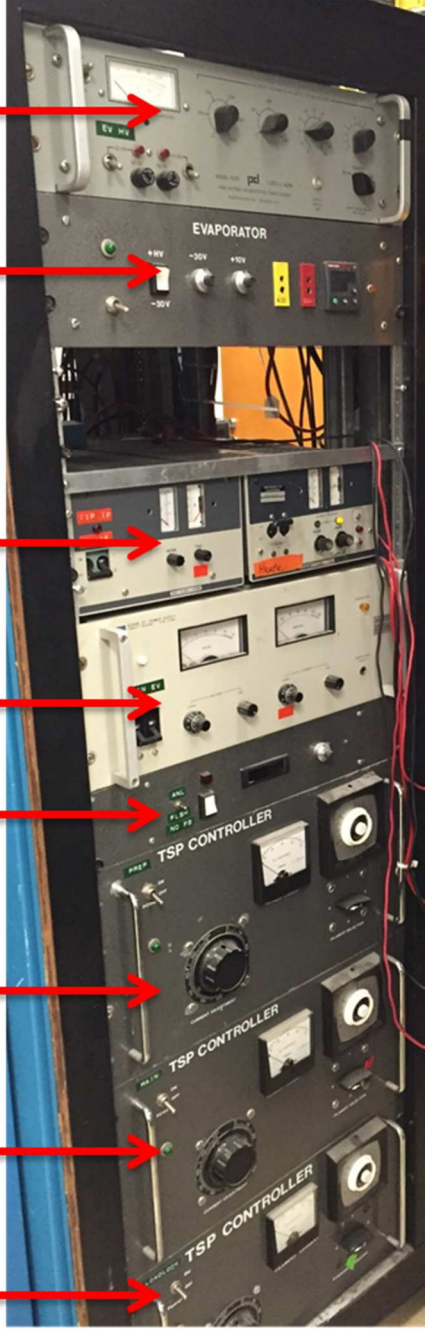
Figure A 6.10: Photo of mk-STM electrical instruments rack #3

Glassman HV

Tip HV
(not in use)

Tip HV

Tip FB Box

HP 6267B
(not in use)

Lock-in
Amplifier
(not in use)

Insert Remote
Controller

220V SLL Ion
Pump Controller

Main Top TSP
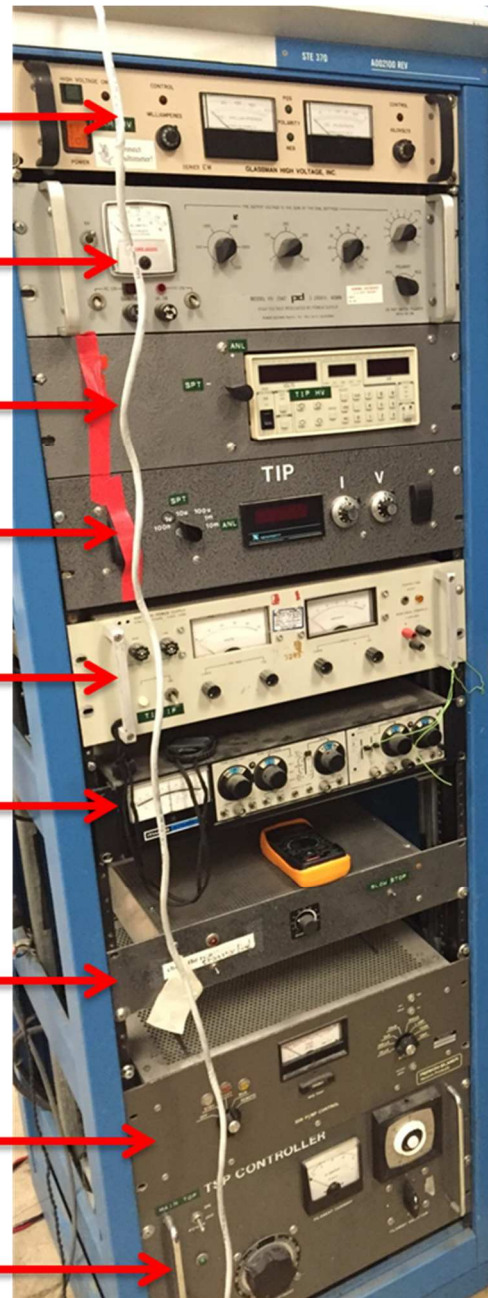
Figure A 6.11: Photo of mk-STM electrical instruments rack #4

Parani Gauge x 5

Cold Cathode
Controller

Small Turbo x 3

AARP x 4

Power
/Pressure
Relay

Emergency
/Normal
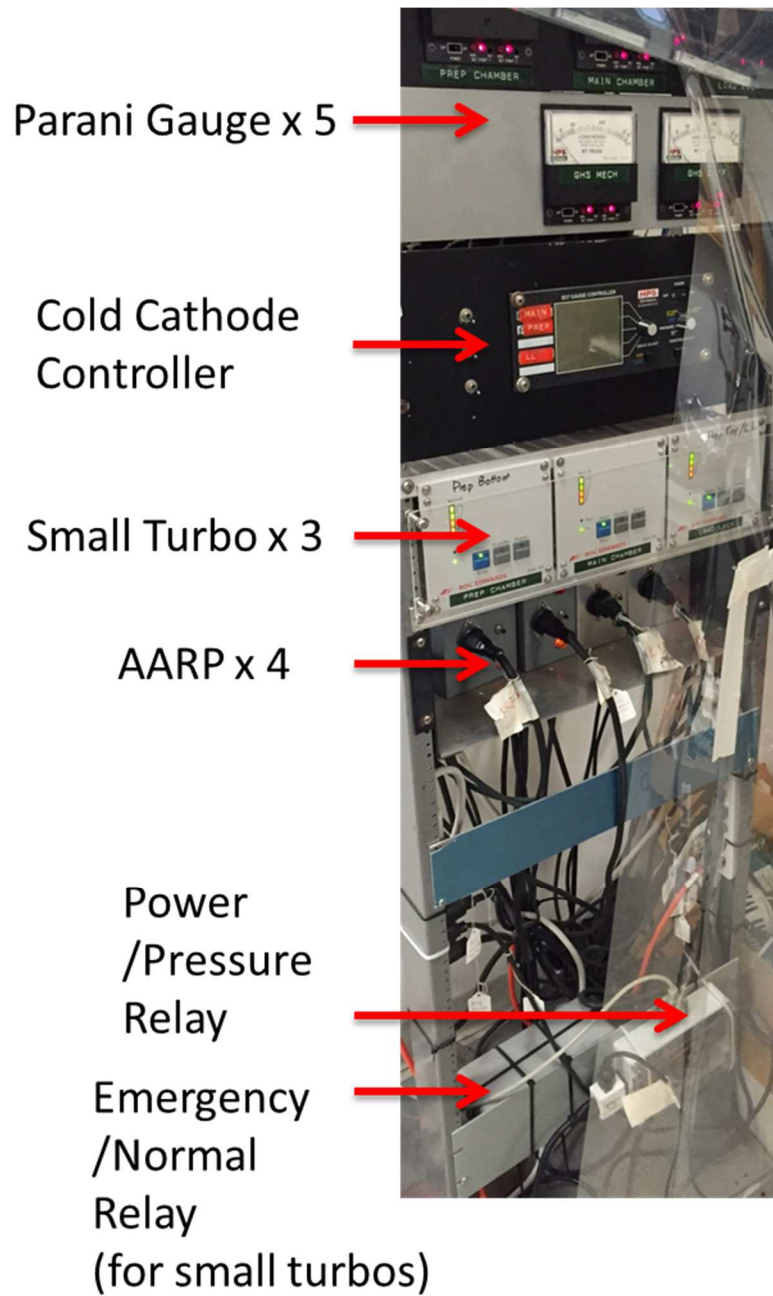Relay
(for small turbos)

Figure A 6.12: Photo of miscellaneous mk-STM electrical instruments
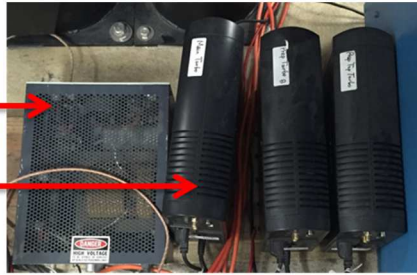
Superconductor
Magnet
Controller

Kethley
DMM(R_{SM})

Fluke DMM
(not in use)

LakeShore TC

TC Monitor(T_{He4-II})

MLL Ion Pump
Controller

Big Turbo
UPS x 3

TC Tip
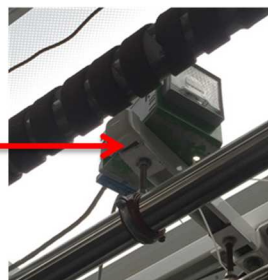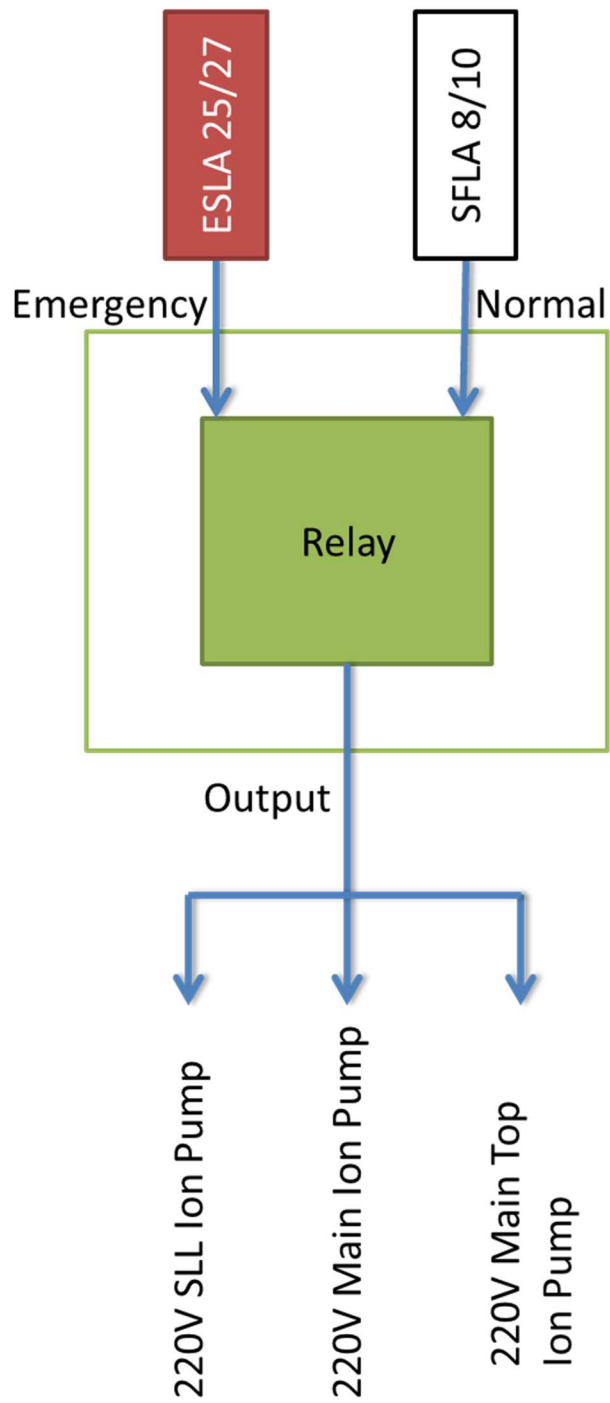Heater

Green
Gauge
(1K pot)

Figure A 6.13: Schematic of mk-STM 220V Ion-pumps power connection

A.7 Pressure and Power Interruption Protection Circuit for mk-STM

The mk-STM Dewar is kept at LHe temperature all year round, in order to avoid contamination due to possible power failure or dry pump failure, a protection circuit controlling two solenoid valves was designed and implemented.

A Pirani gauge sensing the vacuum pressure right after the dry pump controls the activation of the solenoid valve. A J-K flip-flop was designed to sense the rising edge of the signal change from the gauge controller. An improved design that senses two sequential set-points may be used instead.

The control box controls two solenoid valves, in that the newly added solenoid valve is far away from the dry pump. We assume the venting takes time to travel from the failed dry pump to the main turbo pump. And by the time it can reach the big turbo, the newly added solenoid valve after the big turbo is already closed.

An anti-automatic restart protection circuit bought from Amazon was employed for the solenoid valve as a manual restart is expected after a power failure/dry pump failure.

Figure A 7.1 shows the wiring diagram using a J-K flip-flop. The new manual override button is desirable as an add-on feature for next-generation controller.

Again, a design with Arduino board is recommended for any future additions.

Figure A 7.1: Wring diagram version 1.1 for the Pressure and Power Interruption Protection Circuit for mk-STM
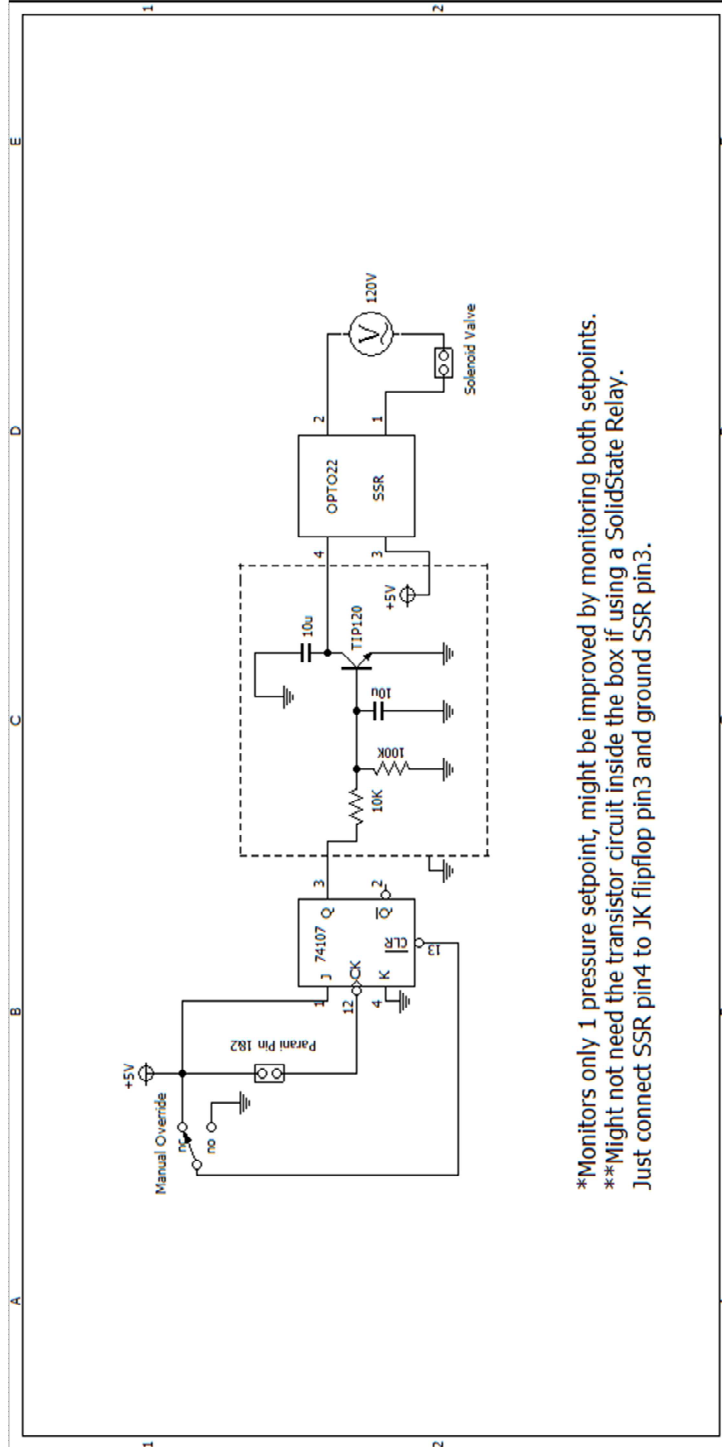
*Monitors only 1 pressure setpoint, might be improved by monitoring both setpoints.
**Might not need the transistor circuit inside the box if using a SolidState Relay.
Just connect SSR pin4 to JK flipflop pin3 and ground SSR pin3.
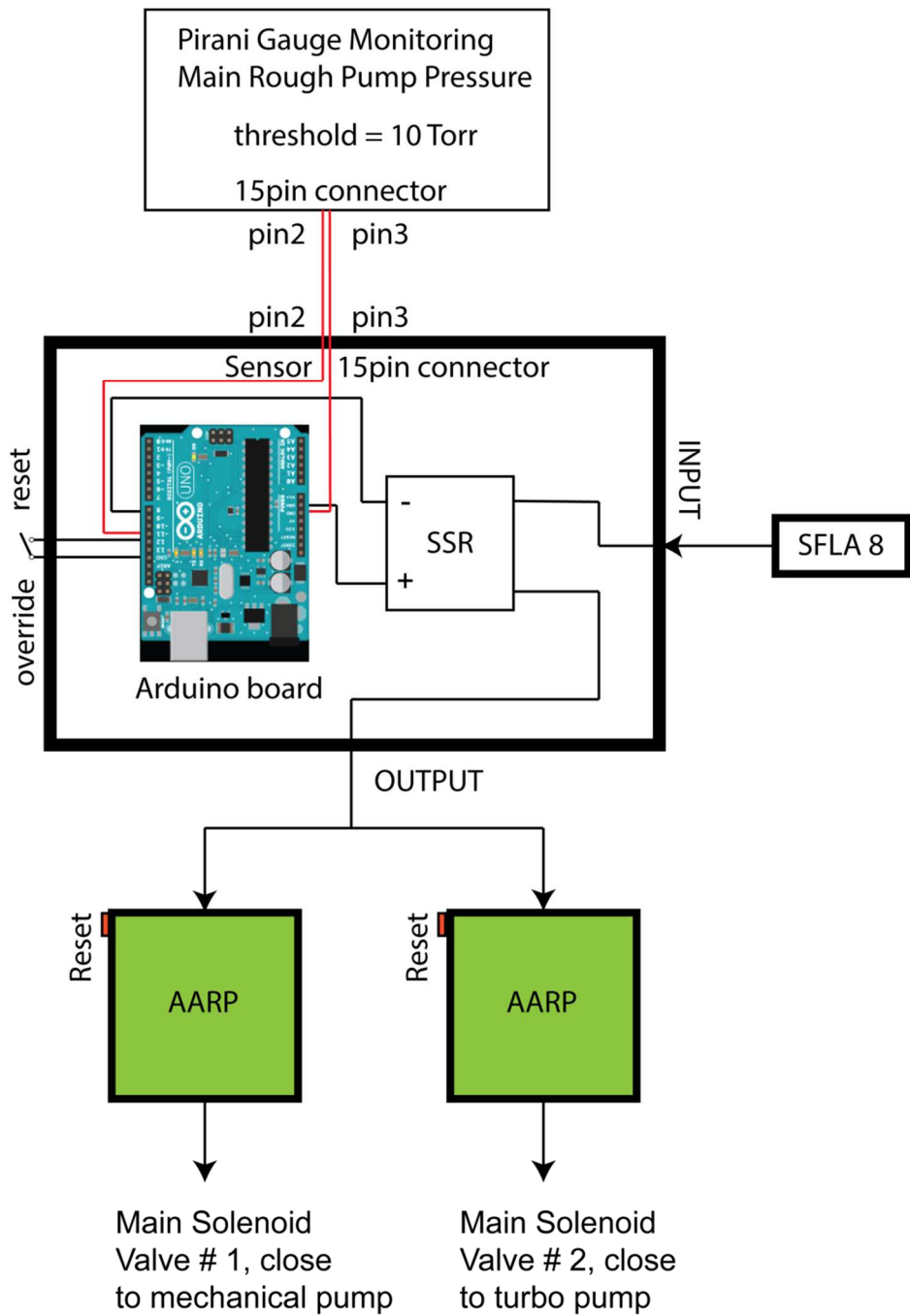
(Update) A new control box using the Arduino board is made by M. Jiang as of Jan. 2016. Refer to his manual in the main server for the details of construction, here I just borrow the schematics of the layout and illustrate the connection between the box and the pirani gauge/solenoid valves etc.

The solenoid valves will be closed if either the power is cut or the pressure at the inlet of dry pump is higher than the threshold set on the Pirani gauge. The solenoid valves will not automatic reopen if the power is recovered or if the pressure falls lower than the threshold again.

1.   To manually open the solenoid valves, one needs to press the 'Reset' button on the control box first, as shown in the top panel in Figure A 7.3.

2.   Before opening the solenoid valves, double check that the mechanical pumps are running and the Pirani pressure is good.

3.   Then, it is recommended to open the two solenoid valves one after another. That is the reason why we have two solenoid valves and each is activated by an AARP respectively.

4.   Open the old solenoid valve closed to the mechanical pump first.

5.   To open it, unplug the connector to the Anti-Automatic Restart Protection (AARP), as shown in Figure A 7.4, and then press the 'Reset' button on the AARP.

6. Then plug the connector back to the AARP. After this, the old solenoid valve will be opened. A valve-opening sound can be heard from the pump room.

7. For the new solenoid valve after the big turbo, there is a new AARP, as shown in Figure A 7.3. Just repeat the same procedure to open this new solenoid valve. By opening these two solenoid valves one after another, one could minimize the risk of possible operation mistakes.

Figure A 7.2: Wring diagram version 2.0 for the Pressure and Power Interruption Protection Circuit for mk-STM

Pirani Gauge Monitoring
Main Rough Pump Pressure

threshold = 10 Torr

15pin connector

pin2   pin3

pin2   pin3

Sensor | 15pin connector

reset

override

SSR

—

+

INPUT

SFLA 8

Arduino board

OUTPUT

Reset

AARP

Reset

AARP

Main Solenoid
Valve # 1, close
to mechanical pump

Main Solenoid
Valve # 2, close
to turbo pump

SSR: Solid State Relay

see manual for more detail

Figure A 7.3: Photos of the Pressure/Power control box and the commercial Anti-Automatic Restart Protection for mk-STM
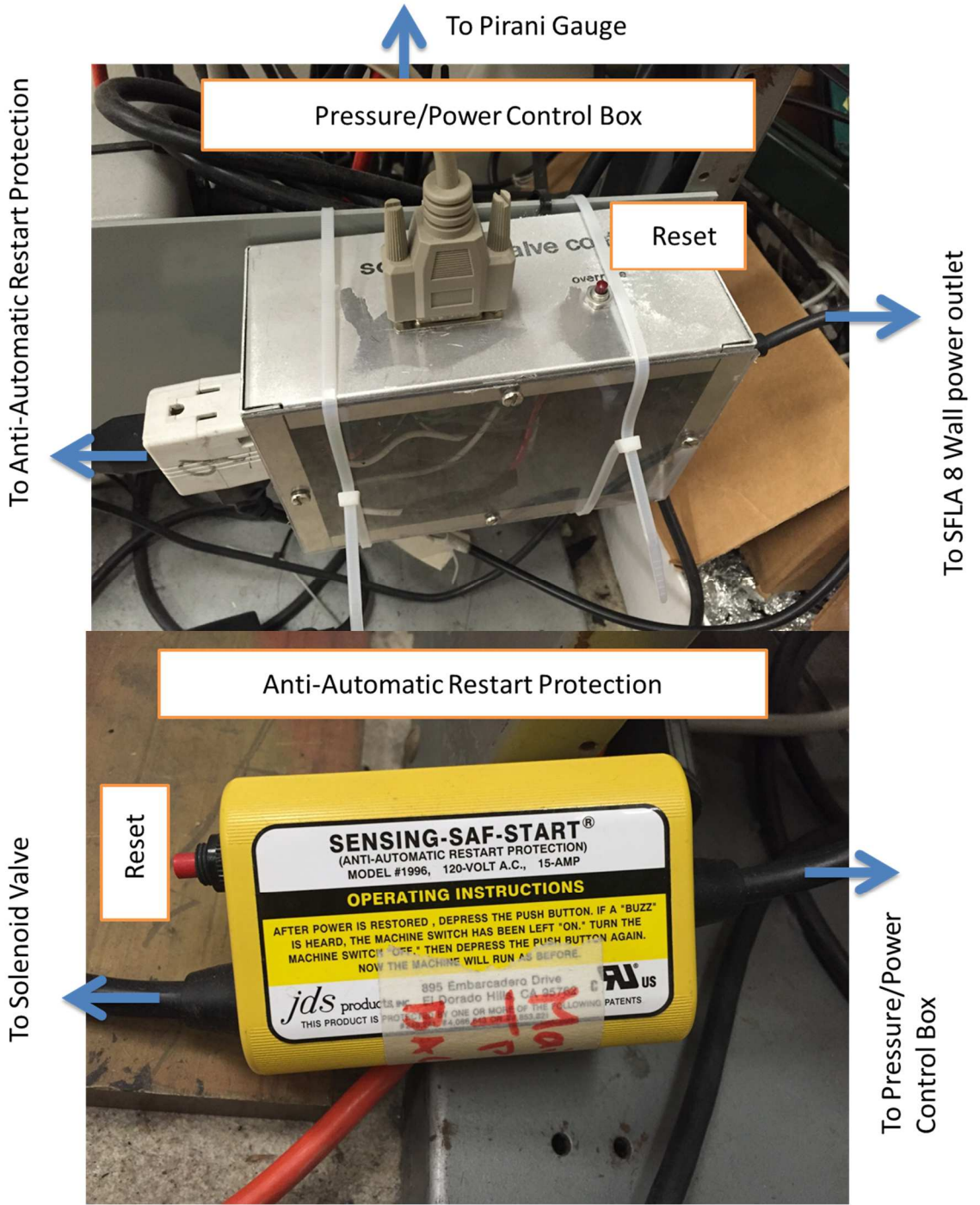
To Pirani Gauge

Pressure/Power Control Box

To Anti-Automatic Restart Protection

Reset

To SFLA 8 Wall power outlet

Anti-Automatic Restart Protection

Reset

SENSING-SAF-START®
(ANTI-AUTOMATIC RESTART PROTECTION)
MODEL #1996, 120-VOLT A.C., 15-AMP

OPERATING INSTRUCTIONS

AFTER POWER IS RESTORED, DEPRESS THE PUSH BUTTON. IF A "BUZZ"
IS HEARD, THE MACHINE SWITCH HAS BEEN LEFT "ON." TURN THE
MACHINE SWITCH "OFF." THEN DEPRESS THE PUSH BUTTON AGAIN.
NOW THE MACHINE WILL RUN AS BEFORE.

895 Embarcadero Drive
jds products inc. El Dorado Hills, CA 95762
THIS PRODUCT IS PROTECTED BY ONE OR MORE OF THE FOLLOWING PATENTS

To Solenoid Valve

To Pressure/Power Control Box

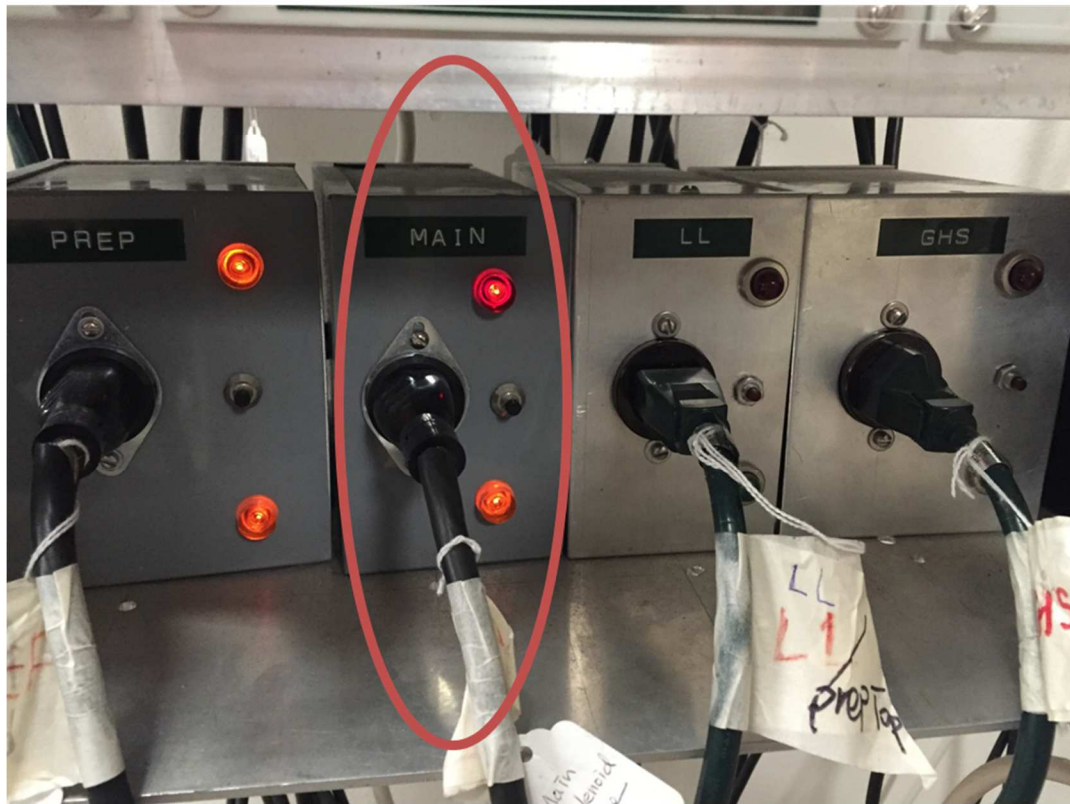Figure A 7.4: Photo of the old Anti-Automatic Restart Protections of mk-STM

Anti-Automatic Restart Protections (old AARP's)

| Prep bottom | Main | SLL | GHS |

A.8 Helium 4 –I Quench Relief Valve Recycling Assembly

Before when we did not recycle helium, the brass relief valve will occasionally get frozen and therefore not functioning as it's intended for. We poked it with stick sometimes to make it release.

Now since we started to recycle helium, the valve is 'sealed' inside the helium gas pathway, in principle no ice will form anymore. But just in case, I designed a simple mechanism to mimic the 'poking' manipulation as we did before, by using a rotary feedthrough, which can pull the centering disk with a string. The loose position is set to be at 0 degree, and by rotating the feedthrough, to about 90 degree, a pressure drop of He4-I dewar pressure can be seen. (Assuming the weak 760torr relief valve is isolated). The rotary feedthrough hits its limit at about 180 degree, stop rotating when you feel resistance.

It helps in situations when you refill Helium4-I where the Dewar pressure can be fine-tuned by setting the rotation angle of this feedthrough, as well as during any experiment with excessive unknown noise, where you can again control the pressure of the Dewar.

Disassembling of the assembly is a bit tricky, the correct steps are as follows:

0. Refrain from removing any KF clamp at the beginning;

1. First, loose the mini flange of the rotary feedthrough;

2. Carefully retrieve the feedthrough, but notice that it is still connected with a string, the other end of which is again glued to the centering disk of the relief valve inside the assembly;

3. So you need to disassemble the string from the tip of the feedthrough now, while holding the feedthrough;

4. As this end of the string is free, you can proceed to remove the rest of the assembly in any order you like.

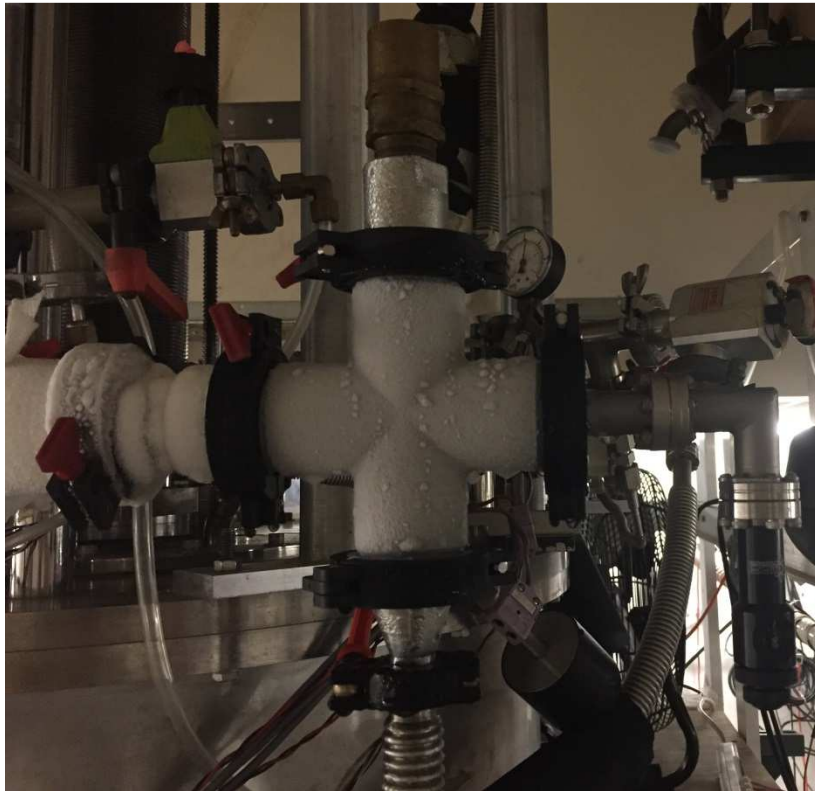Figure A 8.1: Photo of the main exhaust assembly for He4-I in mk-STM

Figure A 8.2: Photo of the rotary feedthrough of the main exhaust assembly for He4-I in mk-STM
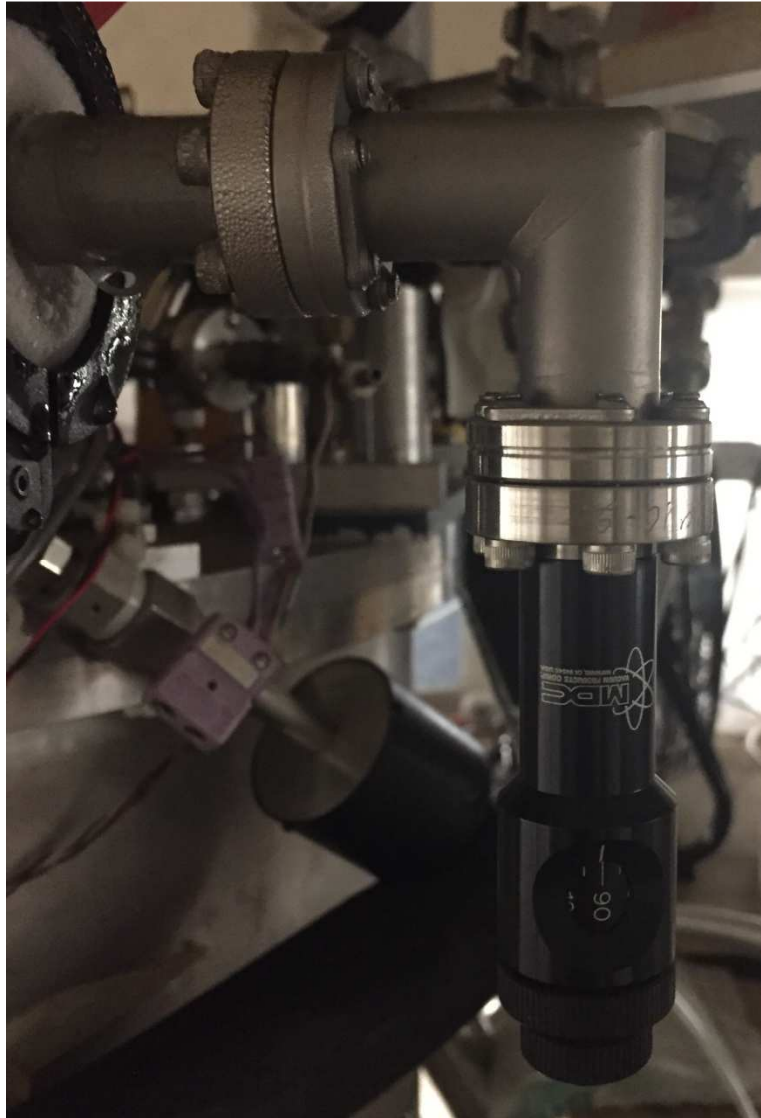
Figure A 8.3: Schematics of the main exhaust assembly for He4-I in mk-STM

800 Torr Big
Relief Valve

Relief To Air

To Recycling

Open   Close